Thesis

Uncertainties in global aerosols and climate effects due to biofuel emissions

Submitted by

John Kelly Kodros

Department of Atmospheric Science

In partial fulfillment of the requirements

For the Degree of Master of Science

Colorado State University

Fort Collins, Colorado

Fall 2015

Master's Committee:

Advisor: Jeffrey Pierce

John Volckens
Sonia Kreidenweis

Copyright by John Kelly Kodros 2015

All Rights Reserved

Abstract

Uncertainties in global aerosols and climate effects due to biofuel emissions

Aerosol emissions from biofuel combustion impact both health and climate; however, while reducing emissions through improvements to combustion technologies will improve health, the net effect on climate is largely unconstrained. In this study, we examine sensitivities in global aerosol concentration, direct radiative climate effect, and cloud-albedo aerosol indirect climate effect to uncertainties in biofuel emission factors, optical mixing-state, and model nucleation and background SOA. We use the Goddard Earth Observing System global chemical-transport model (GEOS-Chem) with TwO Moment Aerosol Sectional (TOMAS) microphysics. The emission factors include: amount, composition, size and hygroscopicity, as well as optical mixing-state properties. We also evaluate emissions from domestic coal use, which is not biofuel but is also frequently emitted from homes. We estimate the direct radiative effect assuming different mixing states (internal, core-shell, and external) with and without absorptive organic aerosol (brown carbon). We find the global-mean direct radiative effect of biofuel emissions ranges from -0.02 to +0.06 W m-2 across all simulation/mixing state combinations with regional effects in source regions ranging from -0.2 to +1.2 W m-2. The global-mean cloud-albedo aerosol indirect effect ranges from +0.01 to -0.02 W m-2 with regional effects in source regions ranging from -1.0 to -0.05 W m-2. The direct radiative effect is strongly dependent on uncertainties in emissions mass, composition, emissions aerosol size distributions and assumed optical mixing state, while the indirect effect is dependent on the emissions mass, emissions aerosol size distribution and the choice of model nucleation and secondary organic aerosol schemes. The sign and magnitude of these effects have a strong

regional dependence. We conclude that the climate effects of biofuel aerosols are largely unconstrained, and the overall sign of the aerosol effects is unclear due to uncertainties in model inputs. This uncertainty limits our ability to introduce mitigation strategies aimed at reducing biofuel black carbon emissions in order to counter warming effects from greenhouse-gases. To better understand the climate impact of particle emissions from biofuel combustion, we recommend field/laboratory measurements to narrow constraints on: 1) emissions mass, 2) emission size distribution, 3) mixing state, and 4) ratio of black carbon to organic aerosol.

Table of Contents

Abstract ii

Chapter 1. Global Modeling 1

1.1. Introduction 1

1.2. Methods 7

1.3. Results 14

1.4. Conclusions 41

1.5. Acknowledgements 43

Chapter 2. Future Work 44

2.1. Cookstove Inventory 44

2.2. Open Trash Burning 45

2.3. Mixing-State Map 46

2.4. Black Carbon Climate Emulator 46

References 48

CHAPTER 1

Global Modeling[1]

1.1. Introduction

Close to half of the world's population relies on combustion of domestic solid fuel use as a source of energy [1], creating concerns for both air quality [2] and climate [3, 4]. Domestic solid fuel combustion in many parts of the world is dominated by biofuel, which includes wood, agricultural waste, animal dung, or charcoal as fuel for domestic energy needs [5, 6]. Biofuel combustion is especially prevalent in developing countries where a significant portion of the population lacks access to electricity or clean combustion technology [1]. Gaseous and particulate matter emitted from biofuel combustion degrades air quality and may lead to detrimental health risks [7]. The recent Global Burden of Disease Study ranks household air pollution from solid fuels and ambient air pollution from particulate matter (all sources) as the third and ninth largest contributors, respectively, to the global burden of disease [8]. Improved combustion devices that reduce human exposure to pollutants should reduce the burden of disease from household air pollution; however, the net climate effect resulting from changing emissions remains uncertain.

Combustion of biofuel emits greenhouse gases (such as carbon dioxide and methane) [9, 10] as well as carbonaceous aerosol particles, such as black carbon (BC) and organic aerosol (OA) [5]. In the atmosphere, carbon dioxide and methane are generally well-mixed due to long lifetimes, and their impacts on climate are better understood than those from aerosols [11]. Conversely, BC and OA have short lifetimes with more complex climate

[1]This chapter from Kodros, J. K., Scott C. E., Farina, S. C., Lee, Y. H., L'Orange C., Volckens, J., Pierce, J. R.: Uncertainties in global aerosols and climate effects due to biofuel emissions, Atmos. Chem. Phys. Discuss., 15, 10199-10256, doi:10.5194/acpd-15-1-2015, 2015. (in review). Ownership is retained by the authors: http://www.atmospheric-chemistry-and-physics.net/general

effects necessitating the use of aerosol microphysical models to understand the net impacts (e.g. [12, 13]). Carbonaceous aerosols can affect climate through scattering/absorbing solar radiation (direct radiative effect), changing the radiative properties of clouds (the cloud-albedo and cloud-lifetime indirect aerosol effects), changing the absorption of snow (snow albedo effect), and changing the temperature profile of the atmosphere (semi-direct effect) [11]. The cloud-lifetime indirect effect, snow albedo effect, and semi-direct effect are more challenging to simulate than the direct effect and cloud-albedo indirect effect; such effects involve changes to meteorology or land surfaces and require fully interactive climate models to elucidate (e.g. [14–16]). In this study, we will be limited to the direct radiative effect and the cloud-albedo aerosol indirect effect but acknowledge that this is not the total aerosol climate forcing.

The direct radiative effect (DRE) refers to direct scattering and absorption of incoming solar radiation [17]. BC has a strong absorbing component while OA is usually considered to be entirely scattering; however, research has shown that under certain combustion conditions OA may have an absorbing component [18–22]. Absorbing OA, commonly termed brown carbon, has a strong wavelength dependence [23], which varies with the BC to OA ratio from combustion [22]. Additionally, the efficiency with which a particle absorbs or scatters solar radiation is dependent on its size [24]. Small particles lack sufficient size to interact efficiently with solar radiation, while large particles will only interact with radiation on the surface of the particle. There then exists a size window (generally, diameters between 100 nm and 1 μm) that maximizes particle mass and surface area to interact with solar radiation most efficiently.

The magnitude of the DRE is strongly dependent on the mixing state of the particles, i.e. do different particle species exist in the same particle or separate particles [25, 26].

Aerosol-climate models generally make assumptions about the mixing state of absorbing BC with scattering species rather than tracking the species mixing explicitly (with some exceptions e.g. [14]). In these models, BC is assumed to be mixed with other particle-phase species in several different ways: homogeneously with scattering species (internal), as a core surrounded by a homogeneously mixed shell (core-shell), or as separate from other aerosol species (external) [27]. In reality, the mixing state lies somewhere in between these assumptions with the mixing state dependent on microphysical processes (e.g. condensation, coagulation), time and location. For a fixed amount of BC and scattering mass, assuming an internal mixture yields the most absorption [27, 26]. There are several methods to estimate the optical properties of a homogenous internal mixture; the most common is to volume weight the refractive indices [28, 29]. Volume weighting the refractive indices decreases the real (scattering) component of the refractive index, while distributing the mass of BC around the entirety of every particle, thus increasing the surface to mass ratio of BC and assigning all particles an absorbing component [24]. This homogenous mixture is thought to be unphysical, but it does give an upper bound on absorption efficiency [28, 27]. The external mixture, where absorbing BC is assumed to be in entirely different particles from scattering species, predicts the least amount of absorption [27]. In an external mixture, only particles with an absorbing component contribute a positive radiative effect [24]. However, this mixing state is also unrealistic in the atmosphere, since processes such as condensation and coagulation contribute to mixing [30–32]. The core-shell morphology, in which a scattering shell surrounds an absorbing BC core, yields less total absorption than the internal mixture assumption but more than the external mixture assumption. The shell acts as a lens that scatters more photons into the absorbing core [33]. This lensing effect amplifies absorption over an external mixture, with the magnitude of the amplification dependent on the core

and shell thicknesses [28]. In the case of absorptive OA, the shell can either absorb or scatter radiation [34]. Bond et al. (2006) estimated that a core-shell morphology would produce an average amplification factor of approximately 1.5 above that of an externally mixed particle. The factor of 1.5 accounts for enhanced absorption due to lensing, which is slightly mitigated by reduced absorption from compacting BC into a spherical core. Modeling studies frequently use the external mixture assumption but multiply the absorption by a fixed enhancement factor (e.g. 1.5 as described above) [35, 36].

The actual magnitude of absorption enhancement by coated BC over externally mixed BC in the atmosphere is uncertain. Mie theory [37] for a concentric scattering shell around an absorbing core predicts a large range of absorption enhancement depending on the thicknesses of the core and shell. Bond et al. (2006) find that for atmospherically relevant particle sizes this enhancement may be as large as 1.9. Theoretical predictions are complicated by the location of the BC core within the particle and the physical structure of the BC particle. The absorption enhancement due to the lensing effect is maximized when the BC core is at the exact center of the particle, and is reduced when the BC is located on the edge [38]. Condensation onto BC may compact the BC agglomerate into a more spherical shape, thus reducing absorption [28, 39]. Additionally, absorption may occur in the shell if the shell is composed of absorptive OA [34]. Laboratory studies have observed absorption enhancements of 1.3 for thin coatings [40] and approximately 2 for thick coatings [41, 39] due to the lensing effect. Field observations have not always agreed with laboratory measurements. Cappa et al. (2012) find absorption enhancements of only 6% over two California regions and suggest this may be caused by BC inclusions at the edge of the particle. Conversely, Wang et al. (2014) find absorption enhancement of 1.8 over China. It is therefore uncertain where and with what magnitude the enhancement of absorption in core-shell mixtures occurs.

The first aerosol indirect effect (AIE), or cloud albedo effect, refers to aerosols altering reflectivity of clouds by changing the cloud droplet number concentration (CDNC) [42]. OA and mixed BC from biofuel combustion can serve as nucleation sites for water vapor, called cloud condensation nuclei (CCN) [30, 13]. Increasing OA and BC concentrations may lead to an increase in CDNC, which will increase cloud albedo and thus yield a negative forcing. The ability for OA and BC particles to act as CCN is a function of particle size and hygroscopicity as well as the maximum supersaturation of water vapor in the cloud [43]. Larger particles can activate into cloud drops more easily than smaller particles (due to higher saturation vapor pressures over curved surfaces); however, larger particles may deplete water vapor concentrations, lower the maximum supersaturation, and limit activation of smaller sized particles.

Emission factors from biofuel combustion are dependent on combustion conditions, which can vary with the type and size of fuel [44, 45], the combustion device [46, 47], and the operator [48]. In general, flaming conditions tend to emit relatively more BC mass and larger sized particles [49] compared to smoldering. Grieshop et al. (2011) finds that the PM emission mass can vary by a factor of four based on different stove and fuel combinations. Wood and agricultural waste emit mostly carbonaceous particles, while coal (used in domestic fuel use but is not biofuel) has a higher sulfur content and so emits more SO_2 gas, which reacts to form condensable H_2SO_4 vapor in the atmosphere that contributes to particle formation and growth. PM mass and composition can vary significantly between different types of technologies used mainly for cooking, heating, or lighting. Additionally, PM emission mass may be dominated during relatively short times of re-fueling and ignition [50]. Variability in emissions factors (including number of users, location of users, stove technology, cooking practices, etc.) can lead to uncertainties in global inventories.

Further complicating biofuel aerosol simulations are that these particles will age in plumes on spatial scales smaller than those resolved by global models. For example, primary organic aerosol (POA) may evaporate and secondary organic aerosol (SOA) may form in woodsmoke plumes [51–53]. Additionally, particle number concentration is decreased by coagulation, which simultaneously increases the mean diameter of the particles [54, 55]. Since the sub-grid processes are not explicitly resolved, models must account for this processing at the emissions stage, which adds additional uncertainty to the number, size and composition of the particles beyond the uncertainties of traditional emissions inventories.

Reducing human exposure to biofuel combustion emissions will likely benefit human health. However, the climate impacts of reducing (or modifying) biofuel combustion are relatively poorly constrained due to the uncertainties described above: emissions amount, size, composition and optical properties as well as uncertainties in other model processes that affect biofuel particles. These uncertainties limit studies aimed at evaluating potential black carbon mitigation strategies from specific sources [56]. In this paper, we quantify the contribution of various uncertainties in biofuel aerosol emissions (emissions rate, composition and size) and model processes (optical mixing state, secondary organic aerosol and nucleation) to the DRE and cloud-albedo AIE. We determine which factors pose the greatest uncertainty to our understanding of how changes to biofuel combustion will affect climate.

In Section 2 we discuss our methods for estimating uncertainties in the climate effects from biofuel. We present modeling results in Section 3. Conclusions and discussions for the results are presented in Section 4.

1.2. Methods

1.2.1. GEOS-Chem-TOMAS overview. We use Goddard Earth Observing System global chemical-transport model (GEOS-Chem) coupled with the TwO Moment Aerosol Sectional (TOMAS) microphysics scheme [57] to calculate aerosol number, mass, and size distributions. This version of TOMAS uses 15 size sections ranging from 3 nm to 10 μm with tracers for sulfate, sea-salt, hydrophobic and hydrophilic OA, externally (pure) and internally mixed (aged) BC, and dust [58, 59]. Conversion from externally mixed OA and BC into internally mixed occurs on a fixed ageing timescale of 1.15 days. We use GEOS-Chem version 9.02 with 4 x 5 horizontal resolution and 47 vertical layers with assimilated meteorology from GEOS5 (http://gmao.gsfc.nasa.gov) to simulate the year 2005.

We use black and organic carbon (OC) emissions from biofuel and other combustion-related sources for the year 2000 from [5]. Anthropogenic fossil fuel emissions are from the Emissions Database for Global Atmospheric Research (EDGAR) inventory [60]. The EDGAR inventory is overwritten in the United States by the Environmental Protection Agency 2005 National Emissions Inventory (NEI05; http://www.epa.gov/ttn/chief/net/2005inventory.html), in Canada by the Criteria Air Contaminants (CAC; http://www.ec.gc.ca/inrp-npri/), in Mexico and the southwestern US by the Big Bend Regional Aerosol and Visibility Study (BRAVO) [61], in Asia by the Streets inventory [62], and in Europe by the Cooperative Programme for Monitoring and Evaluation of the Long-Range Transmission of Air Pollutants in Europe (EMEP) [63]. Residential coal emissions in the Streets inventory are considered separately from biofuel. Open biomass burning (e.g. wildfire) emissions are from the Global Fire Emissions Database version 3 (GFEDv3) [64].

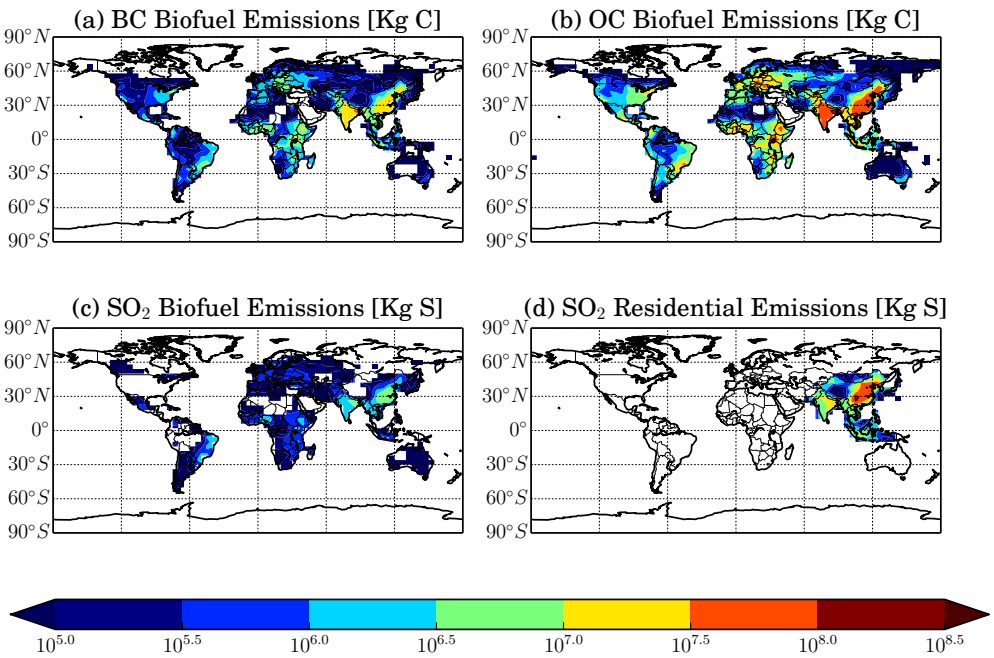

FIGURE 1.1. Annual emissions of (a) biofuel black carbon (BC) and (b) organic carbon (OC) emissions [Kg C] from Bond et al., (2007), (c) biofuel sulfur-dioixde (SO_2) emissions [Kg S] from EDGAR, and (d) residential SO_2 over Asia (in Kg S) from Street's inventory.

Figure 1.1 contains the global annual biofuel BC and OC emissions from Bond et al., (2007) [5] and sulfur-dioxide (SO_2) emissions from EDGAR along with Asia-regional SO_2 emissions from residential coal from the Street's inventory. In other parts of the world, emissions from residential coal use are combined with other sources, and thus we can only isolate this fuel use over Asia. Annual biofuel combustion emissions are 1.6 Tg C per year of BC, 6.3 Tg C per year of OC, and 0.27 Tg S per year SO_2. The emissions of SO_2 from residential coal use in Asia are 1.9 Tg S per year in the Streets inventory. Our lack of isolated global residential coal is a limitation of this study. Northern India and eastern China have the largest aerosol emissions, with substantial contribution from sub-Saharan Africa, South America, and Eastern Europe. In general, biofuel combustion co-emits OC and BC at ratios ranging from 3:1 to 7:1.

1.2.2. Offline direct radiative effect and cloud-albedo indirect effect. The direct radiative effect is calculated offline using the single scatter approximation with the parameterization of Chylek and Wong (1995) [65]. Optical properties are calculated from monthly averaged GEOS-Chem-TOMAS aerosol number and mass distributions with refractive indices for each aerosol species from the Global Aerosol Database (GADs) [66]. We calculate the direct radiative effect using six different assumptions regarding aerosol mixing state (described in Table 1.1): 1) a core-shell mixture with absorptive OA, 2) an internal mixture without absorptive OA, 3) an external mixture with absorption multiplied by 1.5 ('ext*1.5') and with absorptive OA, 4) a core-shell mixture without absorptive OA, 5) an external mixture with absorption multiplied by 1.5 ('ext*1.5') but without absorptive OA, and 6) an external mixture without absorptive OA.

In all mixing states, we assume the particles are spherical. In the internal mixture, all particles within a size bin have the same composition, and the aerosol species are mixed homogeneously within each particle. The refractive index of the sphere is a volume-weighted average of the individual components. In the core-shell calculations, we again assume that all particles within a size bin have the same composition; however, we assume that scattering species (e.g. sulfate and organics) form a shell around a BC core. In our external mixture calculations, we assume that scattering species are separate particles from the BC. Scattering and absorption efficiencies and the asymmetry parameter are calculated using Bohren & Huffman Mie code for homogeneous spheres for the internal and external mixtures and Bohren & Huffman Mie code for concentric spheres for the core-shell mixture [37]. The external mixtures with enhanced absorption use the optical properties of the external mixture with the absorption efficiency multiplied by a factor of 1.5 as described in Bond et al. (2006) [28]. Absorptive OA is simulated using the parameterization of Saleh et al.

Table 1.1. Mixing State Assumptions

Mixing State	Morphology	Refractive Indices	Optical Calculation	Absorptive OA
Core-Shell with absorptive OA	Sphere composed of a homogeneous shell surrounding BC core	Shell components are volume weighted while the core is the refractive index of pure BC	BH Mie code for concentric spheres (BHCOAT)	OA absorption calculated using Saleh et al. (2014) and modeled BC to OA ratio
Internal	homogenous sphere	volume weighted average of individual indices	Bohren and Huffman (1983) (BH) Mie code for homogenous sphere (BHMIE)	None
ext*1.5 with absorptive OA	Aerosol components are mixed internally except BC, which is a separate particle	Volume weighted and pure BC	BHMIE with the absorption efficiency multiplied by a factor of 1.5	OA absorption calculated using Saleh et al. (2014) and modeled BC to OA ratio
Core-Shell	Same as Core-Shell with absorptive OA	Same as Core-Shell with absorptive OA	Same as Core-Shell with absorptive OA	None
ext*1.5	same as ext*1.5 with absorptive OA	same as ext*1.5 with absorptive OA	same as ext*1.5 with absorptive OA	None
External	same as ext*1.5 with absorptive OA	same as ext*1.5 with absorptive OA	BHMIE	None

(2014) [22], which calculates the magnitude and wavelength dependence of the imaginary index of refraction of OA based on the BC to OA ratio.

Our values of the imaginary index of refraction at 550 nm range from 0.05 (based on Saleh et al., 2014 [22]) to 0.006 (the GADs value for non-absorbing OA). Here we use the BC to OA ratio of the model grid box based on all emissions, whereas Saleh et al. (2014) [22] use the BC to OA ratio near the source of emissions only for biomass burning and biofuel emissions. We expect this to introduce some error, however, this method should be sufficient

to show the sensitivity to OA absorption. The DRE is calculated at each grid cell for 5 wavelengths bands (380, 580, 780, 980, 3000 nm) and weighted by the solar spectrum to calculate the broadband DRE. Albedo and cloud fraction are taken as monthly averages from GEOS5. We assume no aerosol effects in columns with clouds, and our all-sky DRE is the clear-sky DRE multiplied by the cloud-free fraction.

We determine the cloud-albedo AIE due to biofuel emissions offline using the radiative transfer model of Edwards and Slingo (1996) [67] with simulated changes to cloud droplet number concentration (CDNC). Our method is described in Scott et al. (2014) [68] and is based on a simplification discussed in detail by Spracklen et al. (2011) [13]. The change in the number of activated particles is calculated using monthly mean aerosol distributions from GEOS-Chem-TOMAS with an activation parameterization, assuming a globally uniform updraft velocity 0.2 m s^{-2}. We calculate cloud droplet number concentrations using the mechanistic parameterization of Nenes and Seinfeld (2003) [69], as updated by Fountoukis and Nenes (2005) [70], which is based on modified Kohler theory. In these calculations, sea-salt and sulfate are assumed to be water soluble and assigned van't Hoff factors of 2 and 2.5 (following Wang et al., 2010 [71]), respectively, when calculating the solute term in the Kohler equation; other components present in each size bin are able to activate when they are internally mixed, which excludes the pure externally mixed BC. The change in CDNC is used to calculate a perturbation to the effective radii of cloud droplets in low- and mid-level (below 600 hPa) water clouds, which in turn leads to a change in net top of the atmosphere radiative flux. We use monthly averaged cloud climatology from the International Satellite Cloud Climatology Project (ISCCP-D2) [72] for the year 2000.

1.2.3. Description of simulations. We test the sensitivity of changes to global aerosol concentration and associated radiative effects due to biofuel emissions and various

Table 1.2. Description of simulations

Simulation	Description
BASE	BC and OA emission mass from Bond et al. (2007); Lognormal size distribution with GMD=100 nm and STD=2.0; Fraction hydrophilic OC=0.5, BC=0.2; ternary nucleation scheme; background anthropogenic SOA on
NOBIOF	All biofuel emissions off; ternary nucleation scheme; background anthropogenic SOA on
MASSX2	BC and OA biofuel emission mass doubled
MASSX0.1	BC and OA biofuel emission mass reduced by 90%
HIGHBC	Biofuel emission BC to OA ratio doubled, while keeping total mass constant
HIGHOA	Biofuel emission BC to OA ratio halved, while keeping total mass constant
SIZE30	Biofuel BC and OA emission median diameter decreased to 30 nm
SIZE200	Biofuel BC and OA emission median increased to 200 nm
SIZENARR	Biofuel BC and OA emission STD decreased to 1.5
SIZEWIDE	Biofuel BC and OA emission STD increased to 2.5
ALLPHILIC	All biofuel BC and OA emitted as hydrophilic
ALLPHOBIC	All biofuel BC and OA emitted as hydrophobic
noSTREET	same as NOBIOF but also with residential SO_2 for Asia from Streets et al. (2003) turned off
BASE_bSOA, NOBIOF_bSOA	Same as 'BASE' and 'NOBIOF' but with anthropogenic SOA turned off
BASE_act, NOBIOF_act	Same as 'BASE' and 'NOBIOF' but with activation nucleation

emission and model assumptions. The 18 simulations used in this study are outlined in Table 1.2. In the model, we must assume effective emissions size distributions that include the effects of sub-grid coagulation that increase the size of the particles (and reduces the number), as we do not explicitly represent coagulation within the plumes on sub-grid scales. In the BASE simulation (our "default" simulation), this assumed size distribution is a single lognormal distribution with a geometric number-mean diameter (GMD) of 100 nm and a standard deviation of 2. Primary OC is emitted in the model as OA with a fixed OA to OC ratio of 1.8. In each grid box, 80% of OA is emitted as hydrophilic and 50% of BC is emitted as internally mixed. Hydrophobic OA and externally mixed BC can age through condensation and coagulation, represented in the model as a fixed timescale of 1.15 days. Nucleation rates are parameterized with binary nucleation in the free troposphere [73] along with a ternary parameterization [74] scaled globally by a 10^{-5} tuning factor [75, 76]. Secondary

organic aerosol (SOA) includes both a biogenic contribution (19 Tg yr^{-1} in GEOS-Chem-TOMAS) and an anthropogenically-enhanced contribution of 100 Tg yr^{-1} correlated with anthropogenic CO emissions [77], following the approach of Spracklen et al. (2011) [78]. In the NOBIOF simulation, BC, OA and SO_2 emissions from biofuel are turned off, while all other emissions remain unchanged. We perform two sensitivity tests regarding emission mass. In MASSX2 and MASSX0.1 the emission mass of OA and BC from biofuel in each grid box from Bond et al. (2007) [5] is doubled and reduced by 90%, respectively. The purpose of increasing the upper bound by a factor of 2 is to explore general uncertainty in the emissions amount, while the lower bound represents a potentially large reduction in emissions due to a changeover in stove technologies [79]. In simulations HIGHBC and HIGHOA, we test the sensitivity to emission composition. The BC to OA ratio is doubled and halved, respectively, while keeping total carbonaceous (BC+OA) mass constant. These bounds incorporate uncertainties due to flaming conditions [32, 48] and OA volatility [80]. We perform four simulations varying the emissions size distribution that include uncertainties not only in the fresh emissions but also in sub-grid aging/coagulation [81, 55]. In SIZE200 we increase the GMD from 100 nm to 200 nm, while in SIZE30 we decrease the GMD to 30 nm. A GMD of 30 nm is more consistent with fresh fossil fuel emissions [82], while a GMD of 200 nm is more consistent with aged biomass burning conditions [55]. We also change the standard deviation of the size distribution from 2 to 1.7 (SIZENARR) and 2.5 (SIZEWIDE). Altering the GMD or width of the size distribution while keeping total mass constant necessitates a change in total number. Finally, we perform two simulations altering the hygroscopicity of emitted BC and OA. In the ALLPHILIC simulation the BC and OA are emitted as hydrophilic, and in the ALLPHOBIC simulation the BC and OA are initially hydrophobic

(but still age to hydrophilic on a fixed timescale). The bounds on hygroscopicity incorporate rapid sub-grid ageing near emission sources [83, 20, 36].

In addition, we run simulations varying certain aspects of the model set-up. In the simulation noSTREET, we re-run the NOBIOF simulation also removing residential SO_2 emissions over Asia. This accounts for coal use in cookstoves and heaters, which is especially prevalent in China [62]. The purpose here is to compare this work to other estimates simulating 'solid fuel' or 'residential' emissions in the regions influenced by emissions from Asia. In other parts of the world, emissions from residential coal use are combined with other emission sources, and thus we can only isolate this fuel use over Asia. In simulations BASE_bSOA and NOBIOF_bSOA, we re-run the BASE and NOBIOF simulations with only biogenic SOA turned on (the anthropogenically enhanced SOA described earlier is turned off). This significantly reduces the background concentration of OA and thus changes the relative importance of nucleation and condensational growth to CCN concentrations [77]. In BASE_ACT and NOBIOF_ACT, we re-run the BASE and NOBIOF with activation nucleation ($J=2*10^{-6}[H_2SO_4]$ [84]; where J is the nucleation rate) instead of the ternary parameterization. The activation parameterization predicts more nucleation over oceans compared to the ternary parameterization, and so this sensitivity test allows us to probe the sensitivity of the interaction of biofuel aerosol with nucleation [76].

1.3. Results

1.3.1. Overview. The global annual impacts of biofuel emissions on aerosol concentrations and the direct and cloud-albedo indirect effects are shown Tables 1.3 and 1.4, and Figure 1.2. Table 1.3 contains percent changes in the boundary layer for the number of particles with diameters greater than 10 nm (N10), greater than 40 nm (N40), greater than 80 nm

Table 1.3. Global, annual-mean percent change in the boundary layer in N10, N40, N80, N150, mass of BC, and mass of OA for the comparisons listed.

Simulation	N10 [%]	N40 [%]	N80[%]	N150[%]	BC Mass [%]	OA Mass [%]
BASE-NOBIOF	0.29	0.93	1.59	2.70	29.5	7.70
MASSX2-NOBIOF	-0.47	1.36	2.95	5.31	59.1	15.4
MASSX0.1-NOBIOF	1.11	0.71	0.55	0.46	2.95	0.75
HIGHBC-NOBIOF	0.35	0.99	1.63	2.74	59.1	6.66
HIGHOA-NOBIOF	0.26	0.90	1.57	2.68	14.8	8.22
SIZE30-NOBIOF	3.60	8.64	10.0	9.61	28.6	7.28
SIZE200-NOBIOF	0.73	0.37	0.28	0.47	29.3	7.60
SIZENARR-NOBIOF	0.16	5.53	10.1	12.2	30.2	7.71
SIZEWIDE-NOBIOF	0.86	0.56	0.48	0.56	27.4	7.07
ALLPHILIC-NOBIOF	0.31	0.95	1.61	2.72	29.5	7.70
ALLPHOBIC-NOBIOF	0.29	0.92	1.58	2.69	29.5	7.70
BASE-noSTREET	1.10	1.78	2.47	3.50	29.5	7.67
BASE_bSOA-NOBIOF_bSOA	-1.19	0.56	2.60	5.11	29.9	23.1
BASE_ACT-NOBIOF_ACT	-0.52	0.30	1.10	2.60	29.53	7.67

(N80) and greater than 150 nm (N150) as well as the mass of BC and OA due to the inclusion of biofuel emissions. Changes in number are cumulative such that N10 includes N40, N80 and N150. N10 is included to illustrate cumulative changes in the total number of particles typically measured in the atmosphere, while N40, N80, and N150 are proxies for climate relevant particles. Percent changes for simulations with perturbations to emission factors are calculated relative to the NOBIOF simulation. Simulations with changes to model set-up are calculated relative to their corresponding NOBIOF simulation (BASE-noSTREET, BASE_bSOA-NOBIOF_bSOA, BASE_ACT-NOBIOF_ACT). Changes to the emission size distribution lead to large changes in particle number, while changes to composition lead to large changes in BC and OA mass.

Table 1.4 contains the global annually averaged DRE and cloud-albedo AIE, relative to NOBIOF, across all simulations and mixing state assumptions. The results of this table

Table 1.4. The global annual-mean all-sky direct radiative effect (DRE) and cloud-albedo aerosol indirect effect (AIE) (in W m^{-2}) due to biofuel for the various comparisons. The direct radiative effect was calculated assuming an internal, core-shell with absorptive OA, core-shell, ext*1.5 with absorptive OA, ext*1.5, and external mixing state (see Table 1.1).

Simulation	Internal	Core-Shell absorptive OA	Core-Shell	ext*15 absorptive OA	ext*1.5	External	AIE
BASE-NOBIOF	0.015	0.021	0.007	0.015	−0.002	−0.008	−0.006
MASSX2-NOBIOF	0.029	0.039	0.013	0.027	−0.004	−0.016	0.002
MASSX0.1-NOBIOF	0.002	0.003	0.001	0.002	0.000	−0.001	−0.014
HIGHBC-NOBIOF	0.047	0.056	0.031	0.045	0.016	0.004	−0.006
HIGHOA-NOBIOF	−0.001	0.002	−0.006	−0.002	−0.011	−0.014	−0.006
SIZE30-NOBIOF	0.008	0.019	0.004	0.015	−0.001	−0.008	−0.021
SIZE200-NOBIOF	0.025	0.023	0.011	0.017	0.002	−0.002	−0.009
SIZENARR-NOBIOF	0.004	0.017	0.002	0.014	−0.002	−0.010	−0.015
SIZEWIDE-NOBIOF	0.025	0.022	0.011	0.017	0.004	0.001	−0.011
ALLPHILIC-NOBIOF	0.015	0.021	0.007	0.015	−0.002	−0.008	−0.007
ALLPHOBIC-NOBIOF	0.015	0.021	0.007	0.015	−0.002	−0.008	−0.006
BASE-noSTREET	0.010	0.016	0.002	0.010	−0.006	−0.012	−0.019
BASE_bSOA-NOBIOF_bSOA	0.013	0.013	0.005	0.008	−0.002	−0.008	0.002
BASE_act-NOBIOF_act	0.015	0.021	0.006	0.015	−0.002	−0.008	0.010

are plotted in Figure 1.2a; the blue bars represent the DRE calculated assuming a core-shell morphology with no absorbing OA, and the cyan bars show the cloud-albedo AIE. The various black symbols represent the DRE from the other assumed mixing states. Globally averaged DRE due to biofuel emissions range from +0.056 to -0.016 W m^{-2}, depending on simulation/mixing-state pair, while the AIE ranges from +0.01 to -0.021 W m^{-2}. Table 1.5

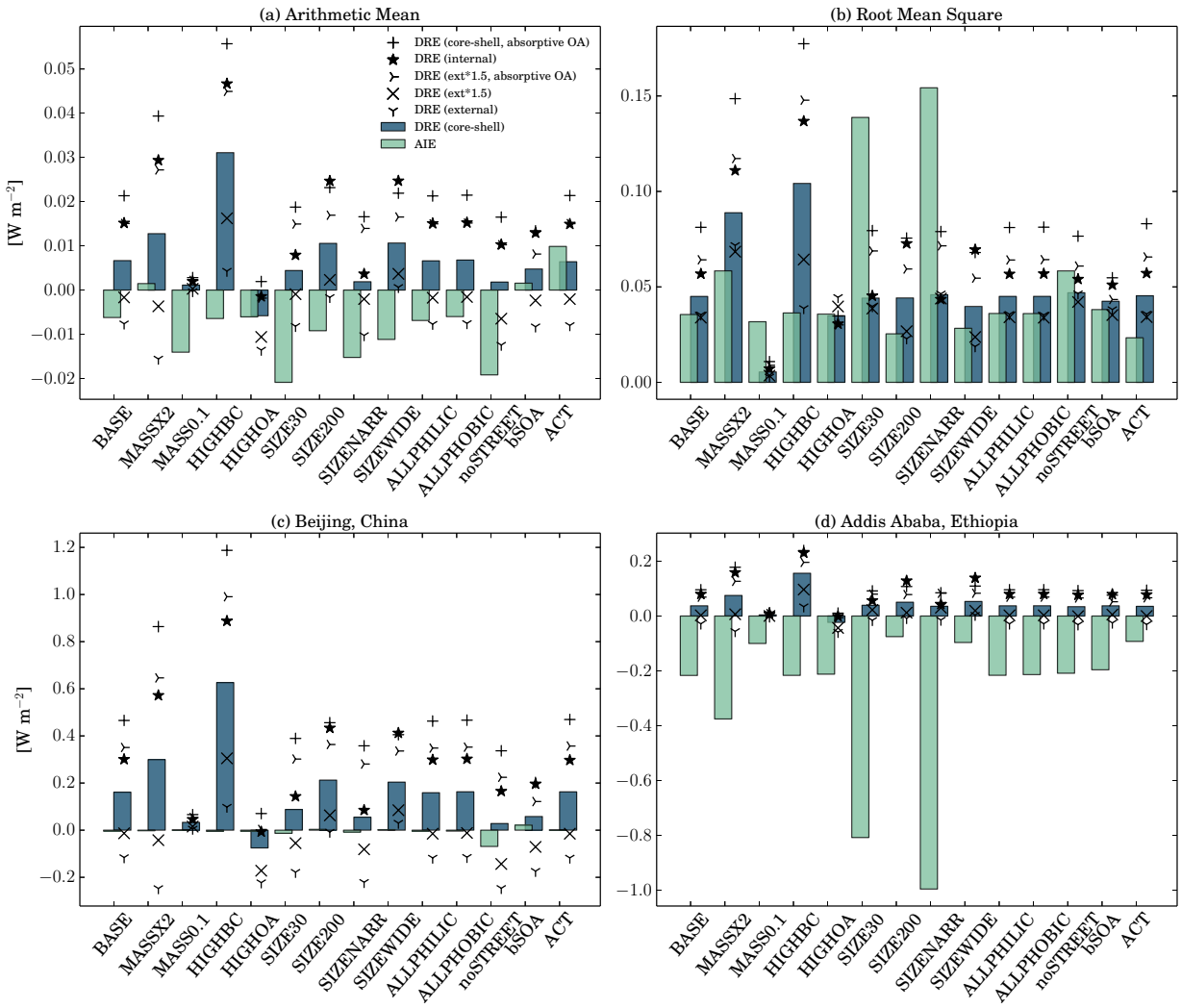

FIGURE 1.2. The DRE and AIE of biofuel aerosol (relative to a NOBIOF simulation) for each simulation as (a) a global arithmetic mean, (b) global root mean square, (c) the value over Beijing, China, (d) the value over Addis Ababa, Ethiopia. The various symbols show alternate mixing state assumptions.

provides a general overview of the key biofuel emissions uncertainties that lead to the largest variability in the DRE and AIE. These uncertainties and complicating factors are shown in detail in the following sections.

Mixing-state and brown carbon vary by region, source category, burn conditions, and atmospheric processing.

Table 1.5. Overview of key uncertainties and complicating factors that drive the variability in the direct radiative effect and cloud-albedo aerosol indirect effect.

Climate Effect	Key Uncertainties	Complicating Factors
Direct Radiative Effect	– BC to OA emission ratio – Emission mass –Optical assumptions (mixing-state and brown carbon) – Emissions size	Mixing-state and brown carbon vary by region, source category, burn conditions, and atmospheric processing.
Cloud-Albedo Indirect Effect	– Emission size distribution – Emission mass	Feedbacks on nucleation/growth create non-linear effects on CCN and indirect effect downwind and aloft of source regions.

The corresponding root mean square (RMS) is shown in Figure 1.2b, which shows the spatial variability of the climate effects. These values are weighted by latitude. The RMS plot indicates absolute model sensitivity to inputs and model parameters tested here; this is important for regional climate effects of changing sign (warming and cooling) that offset each other upon the calculation of a global average. Figures 1.2c and d contain the DRE and cloud-albedo AIE at Beijing, China and Addis Ababa, Ethiopia, respectively. Beijing and Addis Ababa are heavy source regions with different relative magnitudes of the DRE and AIE. We show regional climate effects in order to emphasize that the global mean does not always represent the sign and magnitude of effects in source regions. These figures will be referred to in the following sections.

1.3.2. Overall effect of biofuel emissions under BASE assumptions. To quantify our best estimate of global biofuel emissions impact on aerosol loading and aerosol radiative effects, we run a simulation with default biofuel emissions factors (BASE) and subtract a simulation with biofuel aerosol emissions turned off (NOBIOF). Figures 1.3a and b contain the percent change in BC and OA mass in the boundary layer (annually averaged)

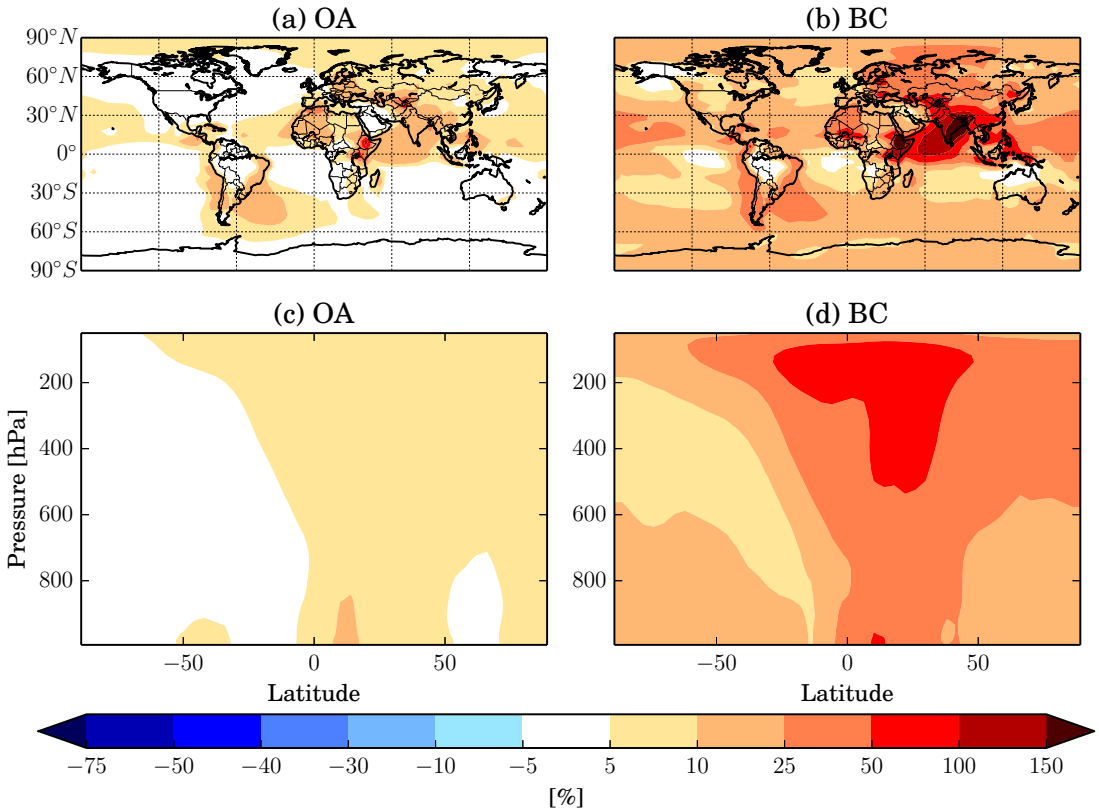

FIGURE 1.3. The percent change in boundary-layer (a) OA and (b) BC mass and (c and d) zonally-averaged with pressure for the BASE-NOBIOF comparison.

due to biofuel emissions. Globally averaged BC mass increases by 30% while OA mass increases by 8%. The largest increases take place in the heavy source regions of India and Ethiopia where biofuel emissions contribute to over half the atmospheric BC mass. Biofuel emissions increase BC mass in most parts of Asia by 25-50%. Central America and the coasts of South America increase BC mass by about 25%. Over oceans, BC mass increases by 10-25%, except on the subtropical west coasts where frequent boundary-layer precipitation occurs. Thus, biofuel emissions are a significant source of BC in both source regions and in remote regions. As OA has additional sources beyond those of BC (e.g. secondary organic aerosol), the fractional increases in OA are smaller than those of BC. Globally-averaged SO_2 mass increases by 0.5% leading to a 0.02% increase in sulfate aerosol (not shown).

Figures 1.3c and d contain zonally averaged BC and OA mass percent changes with pressure level. When biofuel emissions are included, BC and OA mass increases throughout much of the troposphere. Black carbon increases by >25% in the northern hemisphere tropics at all pressure levels. Organic aerosol increases are limited to 5-10% at higher altitudes in the northern hemisphere. Tropical convection lofts BC to high altitudes, which may have implications for the semi-direct and ice cloud effects (not addressed here).

The percent changes in N10 (a), N40 (b), N80 (c), and N150 (d) in the boundary layer, due to the inclusion of biofuel emissions, are shown in Figure 1.4. Changes in N10, N40, and N80 vary by sign and magnitude across different regions resulting in an annual global mean change of 0.29, 0.93, and 1.59% (Table 1.3). Conversely, N150 increases over all land masses with percent changes of over 20% in heavy source regions and an annual global mean increase of 2.70%. The regional decreases in N10, N40, and N80 are caused through a feedback in aerosol microphysics. Biofuel BC and OA emissions (with a median diameter of 100 nm) increase total particle number and thus increase the total aerosol surface area available for condensation. This increased condensation sink leads to (1) lower concentrations of condensable vapors (sulfuric acid and secondary organics), (2) reduced nucleation rates due to reduced sulfuric acid concentrations, (3) slower growth of particles due to reduced condensable vapor concentrations, and (4) increased scavenging of small particles by coagulation due to increases in total aerosol surface area. This feedback is partly mitigated by oxidation of biofuel SO_2 emissions into sulfuric acid, which contributes to nucleation and growth. However, the increased condensation sink from primary BC and OA particles outweighs the contribution of biofuel SO_2 emissions, resulting in a net decrease in sulfuric acid and organic vapors. These factors combine to lower the concentration of small particles in some polluted regions where new-particle formation and growth is a significant contributor

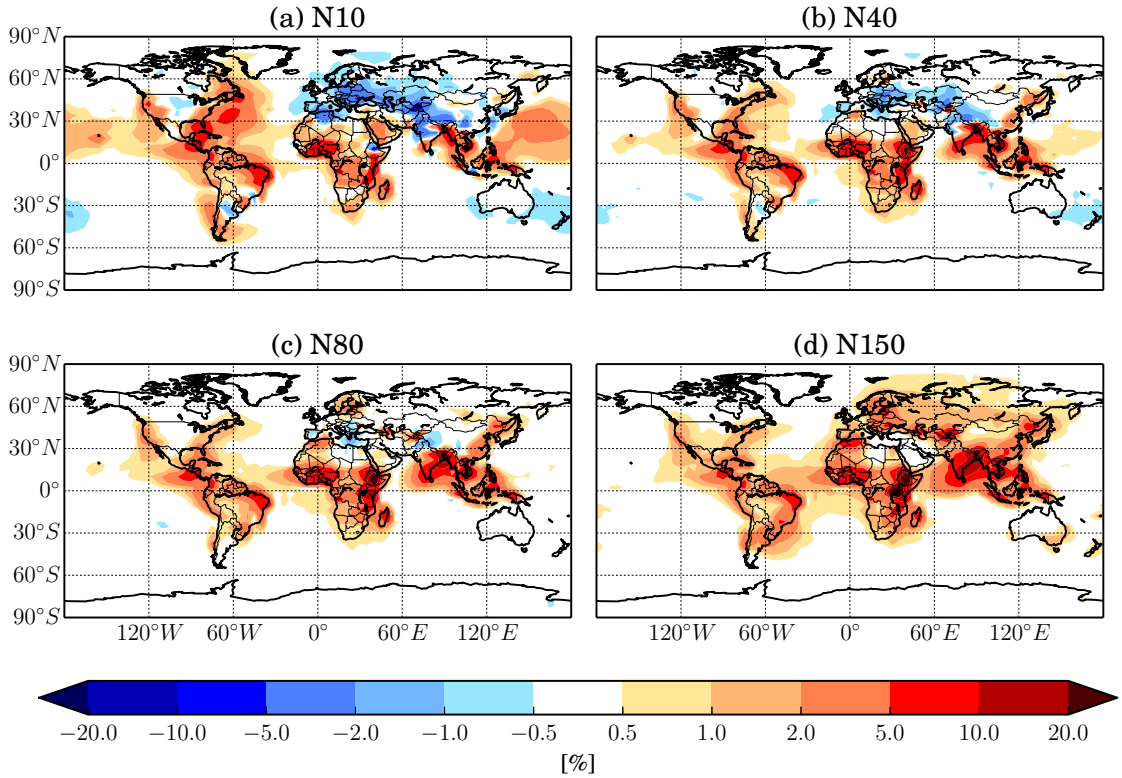

FIGURE 1.4. The annual-mean percent change in boundary layer (a) N10, (b) N40, (c) N80, and (d) N150 for the BASE-NOBIOF comparison.

to particle concentrations. This decrease in N10 reduces the amount of particles able to grow to N40 and N80 sizes. Conversely, sub-Saharan Africa and South America have an increase in all particle sizes. Low initial sulfuric acid concentrations in these areas prevent this microphysical feedback, and therefore addition of biofuel aerosol simply increases the number of particles for all size classes. Finally, biofuel emissions do not significantly change the contribution of particles growing to N150 sizes through condensation, and so suppression of nucleation and condensational growth does not lead to any decreases at this size.

The corresponding zonally averaged percent changes in particle number concentration are plotted in Figure 1.5. In all size classes, particle number concentration tends to increase near the equator and subtropics close to the surface; however, at higher altitudes and away from

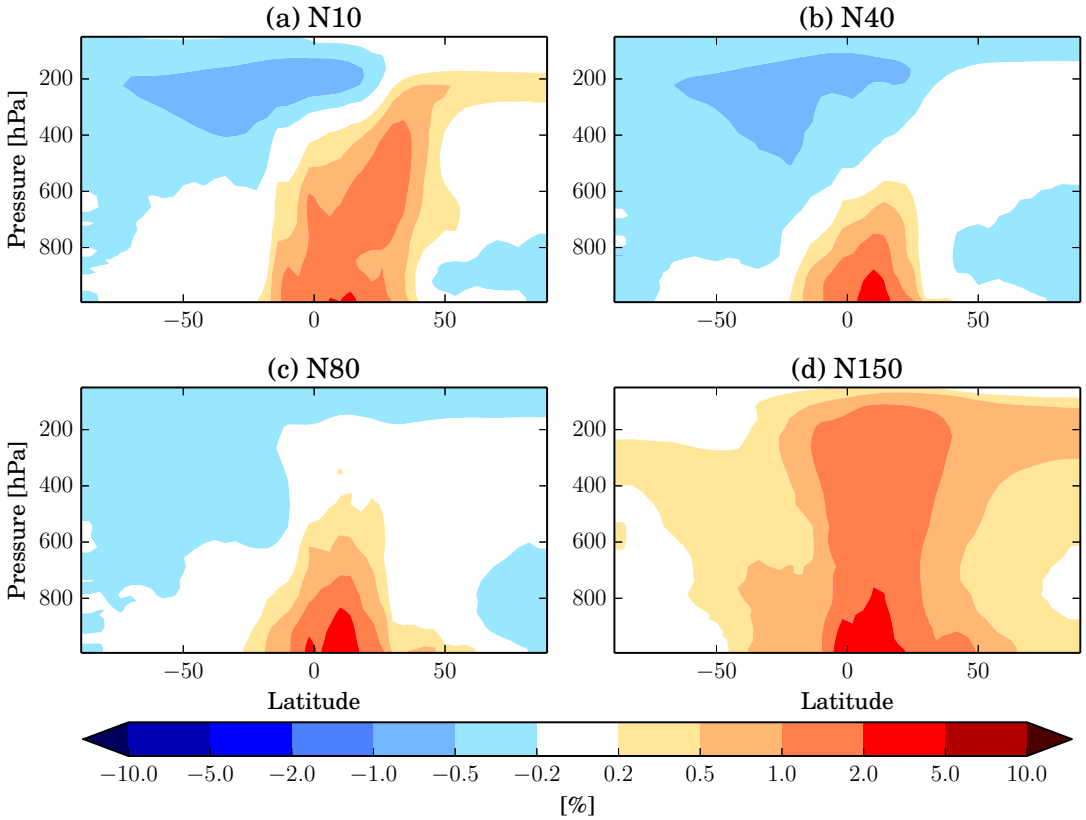

FIGURE 1.5. The annually and zonally averaged percent change throughout the troposphere for (a) N10, (b) N40, (c) N80, and (d) N150 for the BASE-NOBIOF comparison.

source regions N40 and N80 decrease by 0.2-1%. The reason for this is a similar feedback as described above. N40 and N80 are more efficiently scavenged through wet deposition. Near the surface these particles are replaced by primary emissions; however, at higher altitudes condensational growth of nucleated particles is a significant source. With reduced nucleation and condensational growth, fewer particles are able to grow to N40 and N80 sizes. The net result is a decrease in N40 and N80 at higher altitudes. Biofuel emissions do not significantly alter the source of N150 sized particles from condensation growth, and so primary emissions lead to increases in N150 in all locations.

The DRE due to biofuel emissions is shown in Figure 1.6 for the 6 different mixing state assumptions. The global-mean DRE ranges from +0.021 W m^{-2} to -0.008 W m^{-2} (Table

1.4) with strong regional variations across mixing state assumptions. Similar to past global modeling studies the external mixture gives the least absorption and the internal mixture gives the most absorption when absorptive OA is not included [29, 27, 26]. Purely internal or external mixtures globally are not expected to be realistic, but they do give upper and lower bounds on our optics assumptions. The core-shell calculation lies in the middle of our calculated range with an annually averaged global DRE of +0.007 W m^{-2}. The ext*1.5 assumption predicts less absorption than the core-shell assumption, in this case leading to a global negative DRE of -0.002 W m^{-2}. When absorbing OA is included, the DRE becomes more positive. The core-shell morphology with absorptive OA increases the magnitude of the DRE from +0.007 to +0.021 W m^{-2}, which results in the most positive DRE among the cases we consider here. The corresponding ext*1.5 DRE increases from -0.002 without absorptive OA to +0.015 W m^{-2} when absorptive OA is included. Optical assumptions are one of the key uncertainties driving the variability in the DRE. In this study, we estimate the DRE assuming a single mixing state for all grid boxes (with size and composition determined by the concentrations at each location). The mixing state and optical properties of OA likely vary by region and emission source (Table 1.5); however, this is not explicitly explored here.

Different mixing state assumptions also lead to strong variations regionally as well as in the global mean (Fig. 1.6 and Table 1.4), In some regions, such as over China, the DRE can range from a strong positive (over +0.4 W m^{-2}) to negative (less than -0.2 W m^{-2}) in our different sensitivity tests. Some of the regional variability is explained by surface albedo variability. Over bright surfaces, such as the Arctic and Sahara, the DRE is positive in every mixing-state assumption tested. At these locations, the aerosol mixture is darker than the underlying surface across all mixing state assumptions and, therefore, planetary albedo is reduced. Over dark surfaces (oceans), a reduction in aerosol absorption efficiency (by

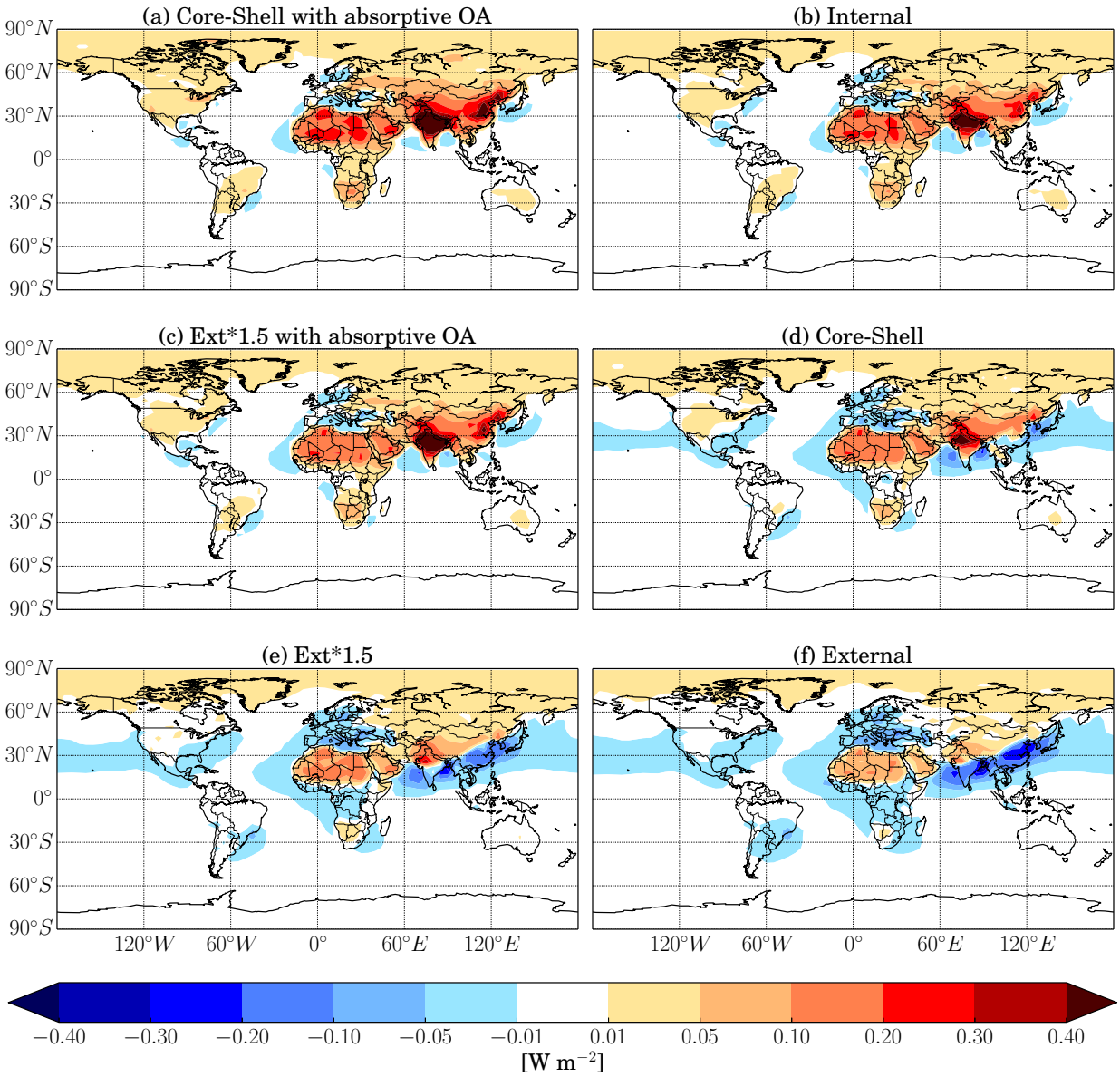

FIGURE 1.6. The DRE for the BASE-NOBIOF comparison assuming a core-shell with absorptive (a) OA (mean: 0.021 W m^{-2}), (b) internal (mean: 0.015 W m^{-2}), (c) ext*1.5 with absorptive OA (mean: 0.015 W m^{-2}), (d) core-shell (mean: 0.007 W m^{-2}), (e) ext*1.5 (mean: -0.002 W m^{-2}), and (f) external (mean: -0.008 W m^{-2}) mixing state.

assuming a different mixing state) makes the aerosol mixture brighter than the underlying surface and, thus, the planetary albedo increases. The negative DRE in eastern China, Southern India, and Europe in the external and ext*1.5 mixing state is a result of the

aerosols increasing the reflectivity over the relatively darker surface, but there is a positive DRE in these locations for the internal mixing state and when absorptive OA is included.

Competing regions of positive and negative DRE limit the magnitude of the globally averaged DRE. Figure 1.2b contains the RMS for the different mixing states and simulations. The RMS represents the absolute model sensitivity of the climate effects to different inputs, accounting for competing regions of positive and negative effects that are not represented in a global-mean. Biofuel combustion contributes changes in the DRE on the order of +/- 0.1 W m^{-2} around the globe. The RMS values for each mixing state are greater than the arithmetic averages; however, the relative order of the magnitude of the mixing states is slightly different. The core-shell with absorptive OA still has the largest value, but now the ext*1.5 with absorptive OA has a noticeably stronger effect than the internal mixture. The ext*1.5 and external mixture have the same strength of forcing, with differing amounts of positive and negative regions.

The cloud-albedo AIE due to biofuel emissions is plotted in Figure 1.7. Biofuel emissions lead to a slight negative in the global mean of the indirect effect of -0.006 W m^{-2}. The magnitude of this global mean is balanced by regional variations. In general the sign and magnitude of the AIE is a competition between increases in CDNC from the biofuel primary emissions and decreases in CDNC from an increased condensation sink of sulfuric acid, organics (suppressing nucleation and growth rates), and water vapor (suppressing supersaturation and activation into CDNC). Biofuel emissions result in a strong negative cloud-albedo AIE in the tropics, specifically in Africa and South America. In this region, the contribution of nucleation and condensational growth to N40 and N80 is less sensitive to the addition of primary biofuel aerosol, and so primary biofuel emissions lead to increases in N40 and N80 from the surface to around 600 hPa (Figure 1.5). The increases in N40 and N80 aloft

lead to increases in CDNC and thus cloud albedo. Conversely, over southern mid-latitude oceans, the reduced nucleation and condensational growth leading to reduced N40 wins out over transported primary emissions leading to a net positive cloud-albedo AIE. This leads to an overall reduction in column CDNC and a positive AIE signal. India and China have both significant primary emissions as well as a strong nucleation suppression feedback, which limits increases in particle number. Additionally, in this region there is strong competition for water vapor and large background aerosol concentrations suppress maximum supersaturation achieved in updrafts. Increases in N150 in this area will further limit the maximum supersaturation, as water vapor will preferentially condense on larger sized particles leaving less available for N40 and N80 sizes. As with the DRE, competing regions of positive and negative values limit the magnitude of the global mean AIE. In Figure 1.2b, the RMS value (0.04 W m^{-2}) for the AIE is much larger in magnitude than the arithmetic mean (-0.006 W m^{-2}). Suppression of condensational growth and of maximum supersaturation in polluted regions explains why the magnitude of the AIE over Beijing (-0.004 W m^{-2}) is much smaller than over the relatively cleaner Addis Ababa (-0.22 W m^{-2}) (Figures 1.2c and d).

1.3.3. Sensitivity of radiative effects to emission mass uncertainties. We test the sensitivity of the direct and indirect effects to primary biofuel particle emissions (BC and OA) to account for uncertainty in measurements, sub-grid ageing, and combustion device improvement scenarios designed to limit particle emissions. Van Donkelaar et al. (2015) [85] find increasing particle emissions in developing countries (China, India, and the Middle East) since 1998, and due to changing emissions, emissions inventories likely carry large uncertainties. Biofuel is a significant emission source in these regions. In MASSX2, we double the BC and OA biofuel emissions mass and compare the results to the NOBIOF simulation. The DRE has a strong dependence on mass and number. Doubling the emitted

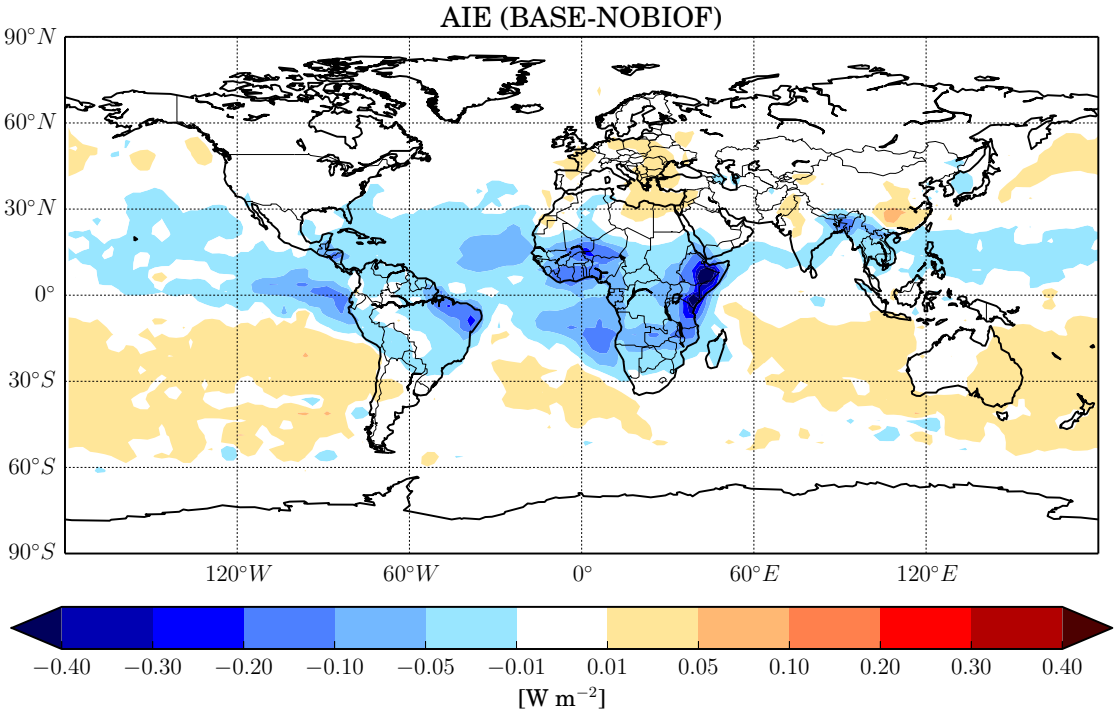

FIGURE 1.7. The cloud-albedo AIE for the BASE-NOBIOF comparison (mean: -0.006 W m^{-2}).

BC and OA approximately doubles the increase in atmospheric concentrations of BC and OA, as well as N80 and N150 relative to the BASE simulation (Table 1.3). This leads to approximately doubling the magnitude of the biofuel DRE for all mixing-state assumptions compared to the BASE-NOBIOF comparison (Table 1.4 and Figure 1.2a). The change in magnitude is in the same direction as the original sign of the DRE, so the external mixture has a larger negative DRE in MASSX2. In MASSX0.1, we emit one-tenth of the BC and OA. The percent change in atmospheric BC and OA mass is roughly one-tenth of the BASE comparison, yet the percent change in number is actually slightly greater than one-tenth of BASE for N80 and N150 (Table 1.3). MASSX0.1 leads to a larger increase in N10 (1.11%) than BASE-NOBIOF (0.29%). MASSX0.1 still increases the number of primary BC and OA particles and thus the condensational sink for sulfuric acid and organics

over NOBIOF; however, there is less suppression of nucleation and growth compared to the BASE simulation. Therefore the relative increase in nucleation and growth relative the BASE comparison offsets some of the reduction in primary emissions (Table 1.3). Ultrafine particles from nucleation have little influence on the mass distribution, and so the large N10 increases have little effect on the DRE. Spatially, these changes are similar to Figure 1.6 and thus are not shown. The globally and annually averaged DRE roughly doubles for MASSX2 and is reduced by one-tenth for MASSX0.1 (Figure 1.2a). This highlights that the total emission mass is a key factor in determining the magnitude of the DRE (Table 1.5). Mixing state assumptions lead to substantial variability in the sign and magnitude in the DRE for MASSX2 (+0.039 to -0.016 W m^{-2}) and change the sign in MASSX0.1 (+0.003 to -0.001 W m^{-2}). In agreement with previous studies, our calculated DRE is roughly linearly dependent on the source emission strength [86, 68].

Conversely, altering emission particle mass has non-linear effects on the AIE of biofuel aerosol. The non-linear effects complicate the response of the AIE (Table 1.5), such that increases in primary emission particle number do not always lead to increases in CCN and cloud reflectivity on a global scale. The AIE for MASSX2-NOBIOF and MASSX0.1-NOBIOF is shown in Figure 1.8. Doubling the biofuel emission mass leads to a globally annually averaged positive cloud-albedo AIE of +0.002 W m^{-2} (compared to -0.006 W m^{-2} for BASE-NOBIOF). The small positive value is a result of regions experiencing a stronger negative cloud-albedo AIE due to added CDNC from primary emissions, which are more than offset by regions experiencing a stronger positive cloud-albedo AIE due to the suppressed nucleation and particle growth. The increased N40, N80, and N150 due to doubled primary emissions (Table 1.3) leads to increases in CDNC near source regions; however, these particle number increases also increase the condensation sink of sulfuric acid and organics, further suppressing

nucleation and particle growth. The result is an increased negative cloud-albedo AIE in Africa and South America where the increases in primary emissions dominate, but increased positive cloud-albedo AIE over oceans where nucleated particles are a significant source for CDNC. The N150 increase occurs throughout the troposphere, so the condensational sink of water vapor increases in already polluted areas of eastern China and Europe, which limits the maximum supersaturation and number of activated particles. On the other hand, reducing emission mass by 90% leads to a globally and annually averaged AIE of biofuel of -0.014 W m^{-2}. MASSX0.1 leads to slight (<1%) increases in N40, N80 and N150 relative NOBIOF. The fewer primary particles in MASSX0.1 suppress nucleation/growth less than in BASE. This allows transported primary BC and OA to compensate for particle reduction from suppressed nucleation/growth downwind and aloft of source regions, leading to increases in CDNC and cloud albedo. In source regions, the reduced primary emissions (relative BASE) are still sufficient to increase CDNC and lead to a slightly negative cloud-albedo AIE locally (-0.05 W m^{-2}). This sensitivity test demonstrates a non-linear relationship between the primary biofuel particle emission mass and the strength of the microphysical feedback as it relates to AIE in the global average. Figure 1.2d shows the AIE in Addis Ababa where changes to CDNC are largely a result of primary emissions. In this location, the changes to AIE are more linear to what we expect from changes in primary emissions only.

In separate experiments (not shown), we test altering biofuel SO_2 emissions mass along with BC and OA. The resulting changes in the cloud-albedo AIE are less than 20% of the changes of altering biofuel BC and OA emissions, suggesting BC and OA emissions are the primary driver of the non-linearity in the AIE.

1.3.4. Sensitivity of radiative effects due to emission composition. Here we test the sensitivity of the DRE and AIE to changes in the BC to OA emission ratio while

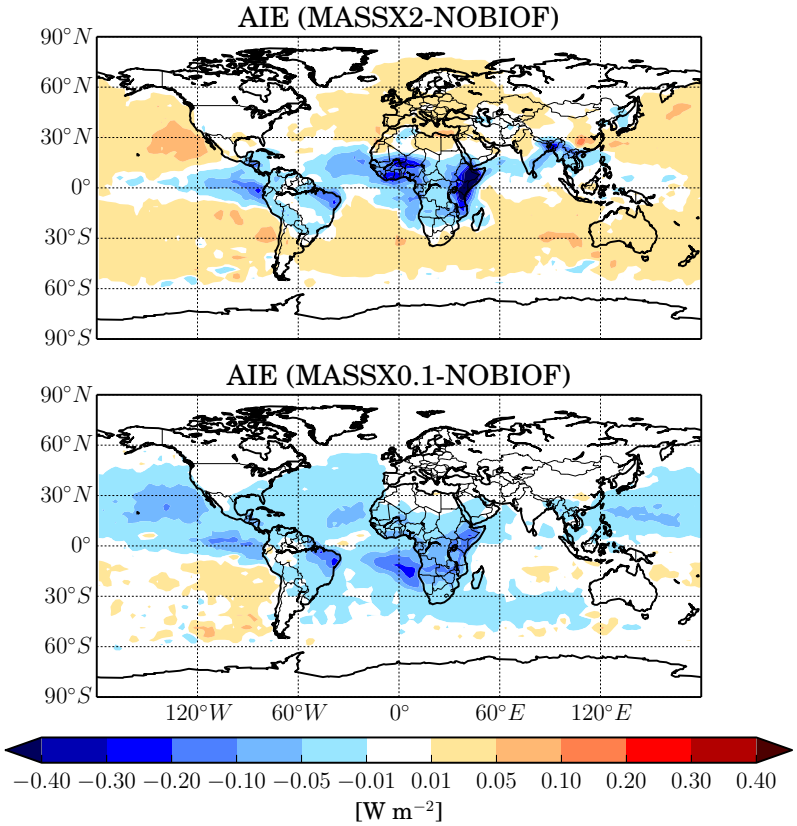

FIGURE 1.8. The AIE for the MASSX2-NOBIOF comparison (top, mean: +0.002 W m^{-2}) and MASSX0.1-NOBIOF comparison (bottom, mean: -0.014 W m^{-2}).

keeping total carbonaceous emission mass constant. This accounts for uncertainties caused by variable flaming conditions and OA volatility. Altering this ratio leads to significant changes in BC and OA concentration; however, since total mass and size remained constant, this has little effect on particle number (Table 1.3). This BC:OA change leads to substantial changes in the DRE, but no change in the AIE (Table 1.4 and Figure 1.2). The HIGHBC simulation increases the percent change in atmospheric BC from 30% in the BASE comparison to 52%. This large increase in BC increases the DRE for all mixing state assumptions. In this comparison all mixing state assumptions give a positive DRE ranging from +0.004 W m^{-2} for the external mixture to +0.056 W m^{-2} for the core-shell with absorptive OA mixture. The HIGHOA simulation increases the concentration of OA, which increases the

scattering component of the aerosol mixture. This leads to a larger negative DRE relative to the BASE simulation. Relative to NOBIOF, the core-shell, ext*1.5 with and without absorptive OA, and the external mixture assumptions now give a negative global mean DRE. There is still enough absorptive OA in the core-shell with absorptive OA to have a small positive global mean DRE.

The cloud albedo AIE is relatively unchanged when increasing or decreasing the emissions BC to OA ratio. Both OA and internally mixed BC can contribute to the number of particles that may activate. In HIGHBC and HIGHOA the number of particles that may activate is similar to BASE. In addition, the hygroscopicity parameter (kappa) changes by less then 0.01 for the HIGHBC and HIGHOA simulations compared to BASE, due in part by our assumption that all species (including non-biofuel species) are internally mixed within each size bin. Thus, the composition change between BC and OA does not greatly change the activation diameters, and so the AIE is unchanged. The patterns in the globally averaged DRE and AIE (Figure 1.2a) are repeated in Figures 1.2b-d, showing there are no strong regional variations in this sensitivity test. Increasing the relative mass of BC results in the largest positive DRE both in the global average and regionally, where in Beijing values range from +0.1 to +1.2 W m^{-2} (Figure 1.2c).

1.3.5. Sensitivity of radiative effects due to emissions size distributions. We test the sensitivity of the DRE and AIE to the emissions size distribution to account for uncertainties in fresh and aged plumes. Changes to the emissions size distributions for BC and OA lead to significant changes in both the DRE and AIE. In simulations SIZE200, SIZE30, SIZEWIDE, and SIZENARR, we change the emission size distribution while keeping emission mass and composition constant (see Table 1.2). However, shifting the emission size distribution while keeping mass constant does necessitate a change in emitted particle

number and surface area. Increasing the number of primary emitted particles may increase the number of CCN near sources, while potentially decreasing the number of CCN downwind and aloft due to suppression of nucleation and growth. The sign of the AIE will depend on the relative effects from primary particles (which increase AIE) versus suppression of nucleation/growth (which decreases AIE). Figure 1.9 contains the change in globally averaged differences in the (a) modeled number distribution, (b) Fuchs surface area distribution, and (c) volume distribution for the BASE-NOBIOF (black line), SIZE30-NOBIOF (blue line with squares), SIZE200-NOBIOF (red line with triangles), SIZENARR-NOBIOF (green line with diamonds), and SIZEWIDE-NOBIOF (magenta line with circles) comparisons. We will use Figure 1.9 below to help understand the climate effects of changing the emissions size distribution.

The total BC and OA emissions mass in these simulations does not change relative to the BASE-NOBIOF comparison (Table 1.3). Altering the emission size distribution does shift the modeled volume/mass distribution relative to the NOBIOF simulation (Figure 1.9c). Increasing the GMD (SIZE200) or increasing the standard deviation of the size distribution (SIZEWIDE) predicts a greater positive DRE relative to the BASE case for all mixing states (Table 1.4 and Figure 1.2a). In these two simulations, the mass distribution is shifted to larger size bins (Figure 1.9c, red and magenta lines), which increases scattering and absorption; however, the fractional increase in the absorption is larger than that for scattering, which lowers the single scattering albedo and leads to a more positive DRE relative to BASE. The opposite is true for SIZE30 and SIZENARR. In these simulations, the mass distribution is shifted to smaller sizes (Figure 1.9c, blue and green lines), causing absorption and scattering to decrease. The fractional decrease in absorption is greater than the fractional decrease in scattering, resulting in a larger single scattering albedo and lower DRE relative to

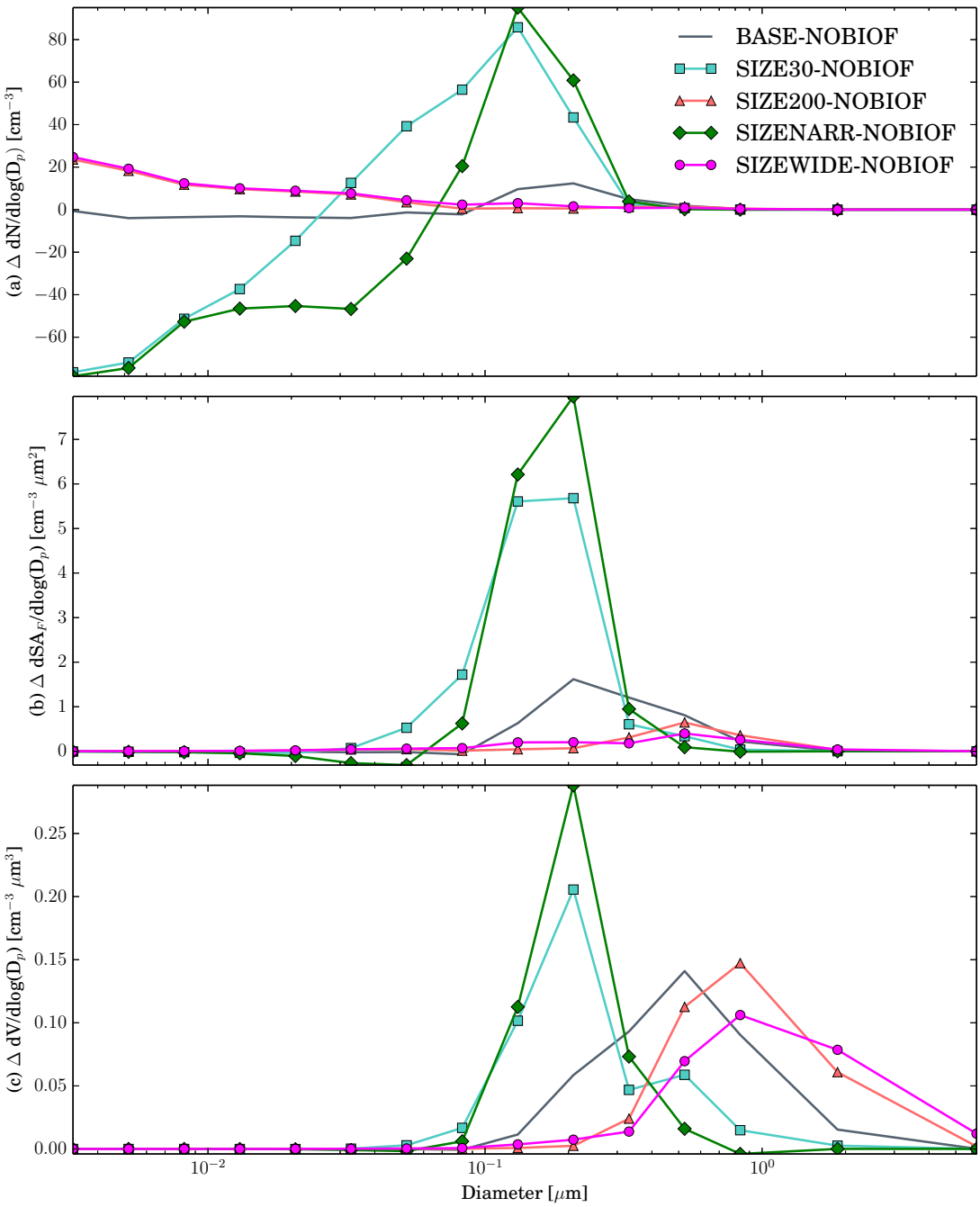

FIGURE 1.9. Globally averaged (a) change in number distribution, (b) change in Fuchs surface area distribution, and (c) change volume distribution for BASE-NOBIOF, SIZE30-NOBIOF, SIZE200-NOBIOF, SIZENARR-NOBIOF, SIZEWIDE-NOBIOF comparisons. The subtractions isolate the contributions of biofuel emissions to each distribution.

BASE. The DRE ranges from positive to negative across mixing states for all size sensitivity simulations except SIZEWIDE, which has a low value of +0.001 W m^{-2}.

Including primary biofuel emissions (BASE) increases the Fuchs surface area (i.e. the condensation sink as a function of size) over NOBIOF (Figure 1.9b, black line), which increases the condensation sink and suppresses nucleation. There is a slight negative change in the number of nucleation mode (<10 nm) particles for the BASE case relative to NOBIOF (Figure 1.9a). The suppressed nucleation from the increased Fuchs surface area is partly balanced by small increases in sulfur dioxide from biofuel combustion, which leads to more nucleation and growth via gas-phase sulfuric acid formation. In SIZE30 and SIZENARR, the increased number of primary emitted particles leads to larger integrated increases in Fuchs surface area compared to BASE-NOBIOF (Figure 1.9b, blue and green lines), leading to a much stronger condensation sink and suppression of nucleation. The net effect is an increase in accumulation-mode particles due to primary emissions and a decrease in nucleation mode particles due to suppression of nucleation compared to the BASE-NOBIOF. Conversely, the decreased number of primary emitted particles in SIZE200 and SIZEWIDE decreases the Fuchs surface area relative the BASE-NOBIOF comparison (Figure 1.9b, red and magenta lines). The unchanged sulfur dioxide emissions combined with reduced Fuchs surface area increase the rate of nucleation and condensational growth. The reduced suppression of nucleation and condensational growth leads to increases in particle number relative the BASE-NOBIOF comparison up to the 100 nm size bin.

The net result is an increased negative AIE for all four size sensitivity simulations relative BASE-NOBIOF. This is caused by either increased primary emitted particle number in source regions (SIZE30 and SIZENARR) or reduced suppression of nucleation and growth (SIZE200 and SIZEWIDE). Thus, the emissions size distribution in the BASE simulation

leads to a lower magnitude AIE than if the size distribution was made larger, smaller, narrower or wider in our model. As with the sensitivity tests due to mass, this shows a non-linear relationship to primary biofuel emissions and the globally averaged cloud-albedo AIE.

Conversely, increasing the number of primary emitted particles relative to BASE (SIZE30 and SIZENARR) does lead to a larger RMS response in the AIE, while reducing the number of primary emitted particles weakens the AIE response (Figure 1.2b). This is because the RMS is dominated by the large cloud-albedo AIE in primary emissions regions. Related to this point, in Addis Ababa (Figure 1.2d) where the microphysical feedback is weaker, increases in primary emitted particle number (SIZE30 and SIZENARR) greatly increase the magnitude of the negative cloud-albedo AIE relative to BASE, and the AIE is reduced relative to BASE when primary emitted number is reduced (SIZE200 and SIZEWIDE). This emphasizes that the global mean does not always capture the sign and magnitude of regional aerosol-climate effects.

1.3.6. Sensitivity to changes in hydrophilicity. Altering the fraction of emitted mass that is hydrophilic caused negligible change in aerosol mass and number (Table 1.3) and in the DRE or AIE (Table 1.4 and Figure 1.2). In this model, conversion from hydrophobic to hydrophilic is represented as a fixed e-folding timescale of 1.15 days. This rapid conversion prevents large changes in number concentration from enhanced wet deposition or cloud droplet activation due to changing hygroscopicity. It is plausible that with online ageing there may be a greater effect, for example if the model included aging timescales which are spatially variable due to the availability of hydrophilic material.

1.3.7. Coal as household fuel. Coal is a common household fuel in some regions of the world and is used for both heating and cooking. Household coal use is especially prevalent in China [87]. Although residential coal combustion is not included in the biofuel inventory used here [5], we include an additional simulation to compare to other studies focusing on the residential sector. In this section, we compare the BASE simulation to a simulation with no biofuel emissions over the globe and no residential coal emissions over Asia (noSTREET) (as mentioned earlier, residential coal emissions outside of Asia are included with other sources in GEOS-Chem and cannot be isolated). Coal generally has a higher sulfur content than the biofuels (Grieshop et al., 2011), and so emits SO_2 along with BC and OA. In GEOS-Chem we are further limited by only being able to isolate residential SO_2 emissions and not BC and OA from coal combustion. The increased SO_2 emissions lead to a stronger scattering component and thus reduced positive DRE across all mixing states. The DRE for the explicit core-shell mixture for BASE-noSTREET is shown in Figure 1.10 (top). The added emissions push the DRE in the negative direction for all mixing states (Figure 1.2a and Table 1.4). Emissions of SO_2 over Asia increase the magnitude of the negative DRE over eastern China and the Indian Ocean. The magnitude of the positive DRE is generally decreased over India and Tibet. Transport of emissions leads to an increased negative DRE throughout the northern hemisphere mid-latitude oceans compared to the BASE-NOBIOF comparison. In Figure 1.2b, the RMS value for the DRE is largely similar to the BASE comparison for the absorptive OA and internal mixing states. This is due to regions of reduced positive DRE being compensated by increased regions of negative DRE. The external, ext*1.5, and core-shell mixtures have a larger RMS value due to an increased negative DRE over China and an increased negative DRE over oceans. The short atmospheric lifetime of aerosol limits the change in DRE. The added coal emissions lead to substantial reduction in the positive

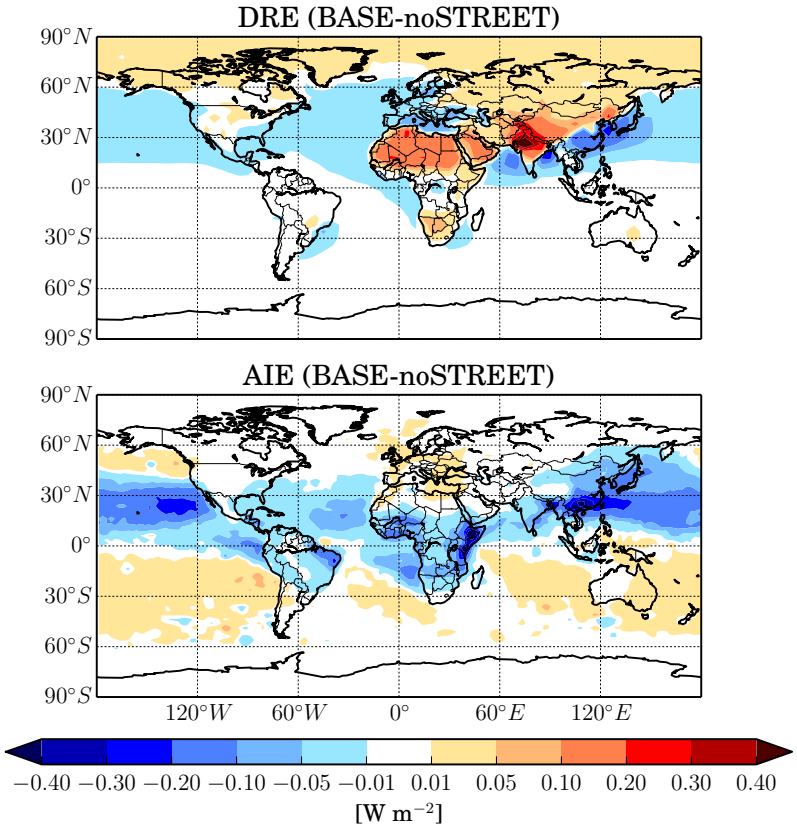

FIGURE 1.10. The DRE assuming a core-shell morphology (top, mean: 0.002 W m^{-2}) and the AIE (bottom, mean: -0.019 W m^{-2}) for the BASE-noSTREET comparison.

DRE over Beijing, but no change over Addis Ababa due to no changes in emissions in Africa (Figure 1.2c and d).

The annually averaged percent change in N40 and N80 in the boundary layer (a and b) is positive throughout all of Asia, with heavy source regions increasing by 10-20% (Figure 1.11). Increases in the Asian region are significantly greater than in the BASE-NOBIOF comparison (see Figure 1.4b and c). Additionally, transported particles lead to increases in N40 and N80 over the Pacific Ocean. Figure 1.11c and d contain the corresponding zonally averaged N40 and N80 percent changes with pressure level. In contrast to the BASE-NOBIOF comparisons (Figure 1.5c and d), addition of household coal use leads to higher increases in N40 and N80 in the Northern Hemisphere tropics and mid-latitudes from the surface to around 200 hPa.

The cloud-albedo AIE for BASE-noSTREET is plotted in Figure 1.10 (bottom). Residential emissions lead to negative cloud-albedo AIE values of -0.2 to -0.4 W m^{-2} locally over eastern China, with transport of N40 and N80 leading to negative effects of -0.1 to -0.3 W m^{-2} over the Pacific Ocean. India also experiences a negative cloud-albedo AIE of at least -0.01 W m^{-2} due to residential emissions. Increased SO_2 mass leads to increases in sulfuric acid concentrations, which can offset the condensational sink caused by primary BC and OA particles. This leads to an increased negative cloud-albedo AIE relative to the BASE-NOBIOF comparison, both in the global arithmetic mean (-0.006 to -0.019 W m^{-2}) and the RMS (0.035 to 0.058 W m^{-2}). The BASE-noSTREET comparison predicts the largest (negative) cloud-albedo AIE for all simulations over Beijing, but similar to the DRE, the cloud-albedo AIE over Addis Ababa is unchanged relative to BASE-NOBIOF (Figure 1.2c and d) due to the lack of emissions changes in Africa.

1.3.8. Changing nucleation and background SOA. To explore the sensitivity of the cloud-albedo AIE to other common assumptions in aerosol microphysics models, we run two simulations that lead to variations in the strength of nucleation/growth feedbacks. In BASE_ACT and NOBIOF_ACT, we use the activation-nucleation scheme, which predicts more nucleation over oceans than the ternary scheme (used in BASE-NOBIOF) because of low NH_3 concentrations over the ocean. Stronger nucleation rates mean a larger source of N40 and N80 from nucleation followed by growth, and modulations to nucleation and growth via changing the condensation sink have larger effects on N40 and N80. Addition of biofuel emissions thus reduces N40 and N80 over oceans in these activation-nucleation simulations more strongly than in simulations with ternary nucleation. The simulations with the activation scheme (BASE_ACT-NOBIOF_ACT) result in decreases in N10 (-0.52%) and smaller increases in N40 (0.30%) and N80 (1.10%) than the simulations with the ternary

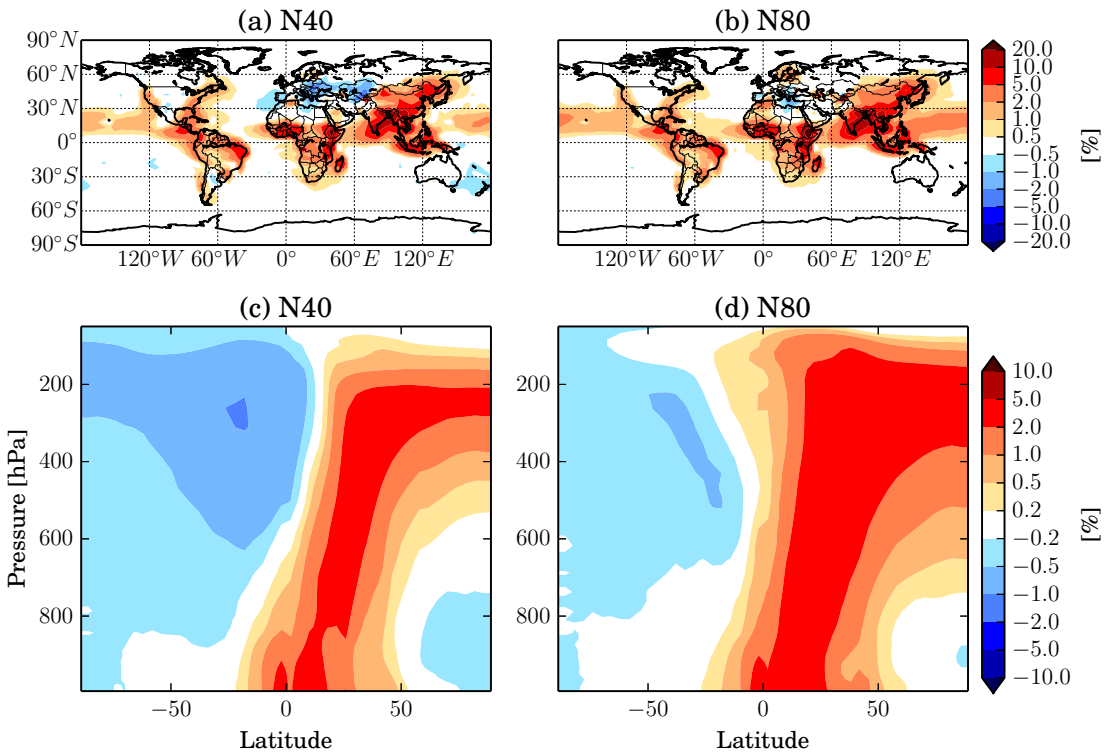

FIGURE 1.11. The percent change for the BASE-noSTREET comparison in boundary layer (a) N40 and (b) N80 and (c and d) zonally-averaged with height.

scheme (BASE-NOBIOF) (Table 1.3). The increased strength of the nucleation/growth feedbacks leads to decreases in CDNC and a positive globally averaged AIE of +0.01 W m^{-2}. The positive AIE is a result of increased regions of positive cloud-albedo AIE over oceans and decreased negative cloud-albedo AIE in source regions. The magnitude of the negative cloud-albedo AIE in Addis Ababa decreases from -0.22 W m^{-2} with ternary nucleation to -0.09 W m^{-2} with activation nucleation (Figure 1.2d). The decrease in the magnitude of the negative AIE in source regions decreases the RMS value (Figure 1.2b), predicting a less strong AIE from biofuel when using activation nucleation than ternary. Changes to nucleation have little effect on the mass distribution and so the DRE change from BASE-NOBIOF is negligible.

We also re-run our BASE and NOBIOF simulations with the 100 Tg of additional anthropogenic SOA [78, 77] turned off (BASE_bSOA and NOBIOF_bSOA, respectively). This leads to significant decreases in background OA concentrations, and it decreases the ability of smaller particles to grow to climate-relevant sizes. Changing background OA reduces the globally averaged DRE due to biofuel emissions, for the core-shell with and without OA and internal mixtures. When biofuel emissions are included in a model without anthropogenic SOA, absorption efficiency is decreased either because there is less OA to mix with the emitted BC (internal), or reduced shell thickness and thus lensing (core-shell). In the case of absorptive OA, biofuel emissions lead to a larger fractional change in OA mass (23.1%), thus reducing the BC to OA ratio more in the bSOA simulations than in the BASE simulation. Since the absorptivity of OA decreases with decreasing BC to OA ratio, assuming mixing states with absorptive OA leads to a lower DRE than in the simulations with anthropogenic SOA. The impact varies regionally such that the reduction in the DRE is more prominent in regions with a larger contribution of anthropogenic SOA, as evident by the difference between Beijing (Figure 1.2c) and Addis Ababa. In addition, lower background aerosol concentrations suggest that biofuel will contribute to a larger fraction of the condensation sink. This results in a stronger suppression of nucleation/growth in bSOA simulations than the BASE comparison. The bSOA simulations result in a larger decrease in N10 (-1.19%) and a smaller increase in N40 (0.56%) from biofuel than the BASE comparison (Table 1.3). On the other hand, lower background concentrations lead to a larger percent increase in N80 and N150. Stronger increases in N150 for the bSOA simulations limit maximum supersaturation over polluted areas of China and Europe leading to fewer activated particles and a positive cloud-albedo AIE (+0.021 W m^{-2} over Beijing, Figure 1.2c). The stronger microphysical

feedback also leads to more areas of positive AIE in southern oceans. The net result is a slight globally averaged positive cloud-albedo AIE of +0.002 W m^{-2}.

1.4. Conclusions

In this paper, we calculate changes to simulated aerosol concentrations in a global model due to the inclusion of biofuel emissions and evaluate the associated direct and indirect radiative effects. We test the sensitivity of these changes to our assumptions about biofuel emissions mass, composition, size and optical properties, as well as model nucleation and background SOA. We find substantial variability in both the sign and magnitude of the globally and annually averaged direct radiative effect (DRE) of biofuel aerosol due to assumptions regarding mixing state across different model simulations. We find the global-mean DRE due to biofuel emissions ranges from +0.06 to -0.02 W m^{-2} considering all simulation/mixing state combinations. The cloud-albedo aerosol indirect effect (AIE) also varies between positive and negative in the global average (-0.02 to +0.01 W m^{-2}). Regionally, the DRE and AIE due to biofuel emissions can also vary substantially (Figures 1.2c and d). In regions of heavy biofuel combustion where background pollution is also high (e.g. Beijing, Figure 1.2c), the DRE can dominate over the AIE. The reduced (and slightly positive) AIE in polluted source regions compared to relatively cleaner regions is a result of an increased condensation sink of sulfuric acid/organics (suppressing nucleation and condensational growth) as well as water vapor (suppressing supersaturation and cloud drop activation). Conversely, in a relatively cleaner source region (Addis Ababa, Figure 1.2d), changes to primary emissions dominate the sensitivity of the AIE. Competing regions of positive and negative cloud-albedo

AIE limit the magnitude of the global average value. Root-mean-squared values, representing the mean absolute magnitude of climate effects, ranges from 0.002 to 0.18 W m^{-2} for the DRE and 0.02 to 0.15 W m^{-2} for the AIE.

Table 1.5 provides a general overview of the key biofuel emissions uncertainties that drive the DRE and AIE response, as well as factors that affect all aerosols that complicate the magnitude of these effects when viewed on a global scale. This study suggests that the direct radiative effect due to biofuel emissions is sensitive to the total emissions mass, emission size distribution, BC to OA ratio, and mixing state assumptions. The cloud-albedo AIE is sensitive to total emissions mass and size distribution because these changes lead to the largest changes in aerosol number concentration (Table 1.5). Additionally, the representation of nucleation and the amount of condensable material (e.g. H_2SO_4 and SOA) in the model leads to non-linear results in the AIE. Carbonaceous aerosol emissions may reduce CCN downwind and aloft of source regions through increasing the condensation sink and suppressing nucleation. Depending on model parameters, this may be enough to balance CCN increases from primary emissions. The non-linear feedbacks complicate the AIE response to changes in primary emissions (Table 1.5). Additionally, including residential coal leads to large changes in the DRE and cloud-albedo AIE compared to model simulations with just biofuel emissions. In this paper, we only turn off residential coal over Asia (in the noSTREET simulation), and so considering the 'residential sector' on a global scale may yield different results than modeling only biofuel emissions.

As population and the demand for accessible energy increases in developing countries, particularly in Asia and Africa, the need for cleaner more efficient combustion devices will increase. While successful technologies will improve air quality and reduce climate impacts from greenhouse gases, the aerosol effects on climate from these source improvements are

poorly constrained. Based on the results of this paper, we find that more measurements are needed on the following properties in order to better constrain the climate impacts of biofuel aerosol in global models:

(1) Total emissions mass

(2) BC to OA ratio

(3) Emissions size distribution (including the effects of sub-grid aging/coagulation)

(4) Mixing state for optical calculations

Without better constraints, even the sign of the net global aerosol effects is uncertain. Previous work has suggested that reducing BC emissions from biofuel sources may be used as a means of countering greenhouse-gas warming effects [88]; however, if these suggested aerosol controls include removing both the OA and BC emissions from biofuel sources, it is unclear if a net global cooling will be achievable based on the range of our results.

1.5. Acknowledgements

This research has been supported by a grant from the U.S. Environmental Protection Agency's Science to Achieve Results (STAR) program through grant #83543801. Although the research described in the article has been funded wholly by the U.S. Environmental Protection Agency's STAR program, it has not been subjected to any EPA review and therefore does not necessarily reflect the views of the Agency, and no official endorsement should be inferred. We thank Bonne Ford for useful feedback on the manuscript.

CHAPTER 2

Future Work

2.1. Cookstove Inventory

The results of this thesis demonstrate a need for a more detailed cookstove inventory, especially with regards to aerosol mass, size, and optical properties that depend on stoves and fuels. I propose to create a global cookstove-specific emissions inventory. This inventory will consider emission factors for greenhouse gases (CO_2, CO, CH_4), VOCs, and size and composition-resolved primary aerosol emissions. Emission factors will be taken from on-going laboratory and field studies at Colorado State University. Emission factors will be combined with gridded population and fuel use estimates from literature (e.g. [6, 62]). One notable improvement of this inventory over past studies will be the inclusion of size-resolved aerosol emissions. Size-resolved emissions will reduce one of the main uncertainties related to biofuel and cookstove emissions. We will also include information of sub-grid aging from experiments conducted at Carnegie Mellon University. This inventory will be incorporated into global atmospheric models to assess global climate and health impacts of cookstoves.

In reality, emission variabilities exist due to stove user, fuel availability, and stove aging [48]. I can address this in the inventory by creating probability distributions for emission mass, aerosol median diameter, and width of the aerosol size distribution.

In building this inventory I will create tools needed to manipulate the 'standard' inventory, allowing for the creation of alternate inventories. For example I could create an emission inventory based on future population and fuel use projections but with the same traditional stoves predominantly used today. The ability to create alternate inventories will allow us to asses the climate and health impacts of hypothetical improvement scenarios. We

can use a Monte Carlo method to randomly assign stove and fuel improvements by region, creating thousands of hypothetical future emission scenarios. This will allow us to consider what regional improvements result in the optimal changes for climate and health.

Additionally, this global inventory can be combined with region specific inventories. We can take detailed inventories for a specific region (for example Dr. Christine Weidinmyer is creating a detailed, high-resolution inventory for Ghana) and overwrite our emissions in that region with the region-specific inventory. This will allow for high resolution regional modeling, with boundary conditions provided by our global inventory.

2.2. Open Trash Burning

In addition to the domestic emissions explored in this thesis, there are other energy-related combustion emissions that affect climate and air quality in developing regions. One such emission source is the combustion of trash. Open waste and trash burning takes place in impoverished urban and rural settings where insufficient infrastructure exists to properly dispose of waste. This issue is especially prevalent in rapidly growing populations [89]. Dr. Christine Wiedinmyer has developed a global trash burning inventory [90]. Black and organic carbon emissions from this inventory are comparable in magnitude to the biofuel emissions in this study. I propose to include these emissions into GEOS-Chem-TOMAS to estimate the global climate effects from trash burning emissions. For this project, I will update our method of estimating the direct radiative and cloud albedo indirect aerosol effects. I will use an offline version of the Rapid Radiative Transfer Model for GCMs, which includes multiple scattering and stochastic 3D cloud properties (which our current method lacks). This work will further our understanding of energy-related carbonaceous emissions' role as a climate forcer. I will co-advise a summer student this summer who will work on this project.

2.3. Mixing-State Map

One of the largest factors affecting the magnitude of the direct radiative effect is optical mixing-state. Past modeling studies find a difference of 0.5 W m^{-2} in the direct radiative effect when assuming an internal mixture over an external mixture [29, 26]. The work in this thesis finds assumptions regarding mixing state alter the sign and magnitude of the direct radiative effect from biofuel combustion both in the global mean and regionally. For computational efficiency, many studies assume a globally uniform mixing state of either completely externally or internally mixed aerosols [28, 36]. In reality, the mixing state may vary substantially by region and there may be degrees of mixing [91]. I purpose to create a spatial map of mixing state index (an index describing the degree of mixing [92] for use in calculating the direct radiative and cloud-albedo indirect effect. Collaborating with Dr. Riemer's group at Univ. Illinois, we can use a lagrangian column single particle model to actively model bulk particle and single particle diversity along the column trajectory. We will supply aerosol initial conditions (from GEOS-Chem-TOMAS simulations) and aerosol emissions. We can then estimate the direct radiative and cloud-albedo indirect effect based on the degree of mixing in each grid cell. Furthermore, by isolating certain emission sources we can quantify the contribution to particle mixing from specific sources (i.e biomass burning, coal power plants, etc).

2.4. Black Carbon Climate Emulator

A number of studies have suggested mitigation of black carbon to counter warming effects from greenhouse gases; however, large uncertainties exist in the sign and magnitude of the net black carbon climate forcing. I propose to build an emulator to explore a larger parameter space involving black carbon emissions and climate forcings. The uncertainty space tested

will include the emission aerosol size distribution, emission mass, subgrid aging, optical properties, and co-emitted species. The emulator will be built using output from GEOS-Chem-TOMAS. The results of this study will quantify the uncertainty in climate forcing associated with each parameter. This work will inform decision makers on the likelihood of black-carbon control strategies improving climate.

References

[1] N. Bruce, R. Perez-Padilla, and R. Albalak, "Indoor air pollution in developing countries: A major environmental and public health challenge," *Bulletin of the World Health Organization*, vol. 78, no. 9, pp. 1078–1092, 2000.

[2] N. Bruce, E. Rehfuess, S. Mehta, G. Hutton, and K. Smith, *Indoor air pollution, Disease Control Priorities in Developing Countries*. New York: Oxford University Press, 2nd ed., 2006.

[3] T. Bond, C. Venkataraman, and O. Masera, "Global atmospheric impacts of residential fuels," *Energy for Sustainable Development*, vol. 8, pp. 20–32, Sept. 2004.

[4] C. Venkataraman, G. Habib, A. Eiguren-Fernandez, A. H. Miguel, and S. K. Friedlander, "Residential biofuels in South Asia: carbonaceous aerosol emissions and climate impacts.," *Science (New York, N.Y.)*, vol. 307, pp. 1454–1456, 2005.

[5] T. C. Bond, E. Bhardwaj, R. Dong, R. Jogani, S. Jung, C. Roden, D. G. Streets, and N. M. Trautmann, "Historical emissions of black and organic carbon aerosol from energy-related combustion, 1850-2000," *Global Biogeochemical Cycles*, vol. 21, June 2007.

[6] S. D. Fernandes, N. M. Trautmann, D. G. Streets, C. a. Roden, and T. C. Bond, "Global biofuel use, 1850-2000," *Global Biogeochemical Cycles*, vol. 21, June 2007.

[7] S. Akbar, D. Barnes, A. Eil, and A. Gnezditskaia, "Household Cookstoves, Environment, Health, and Climate Change: A New Look at an Old Problem." 2011.

[8] S. S. Lim, T. Vos, A. D. Flaxman, G. Danaei, K. Shibuya, H. Adair-Rohani, M. Amann, H. R. Anderson, K. G. Andrews, M. Aryee, C. Atkinson, L. J. Bacchus, A. N. Bahalim, K. Balakrishnan, J. Balmes, S. Barker-Collo, A. Baxter, M. L. Bell, J. D. Blore, F. Blyth, C. Bonner, G. Borges, R. Bourne, M. Boussinesq, M. Brauer, P. Brooks, N. G. Bruce, B. Brunekreef, C. Bryan-Hancock, C. Bucello, R. Buchbinder, F. Bull,

R. T. Burnett, T. E. Byers, B. Calabria, J. Carapetis, E. Carnahan, Z. Chafe, F. Charlson, H. Chen, J. S. Chen, A. T.-A. Cheng, J. C. Child, A. Cohen, K. E. Colson, B. C. Cowie, S. Darby, S. Darling, A. Davis, L. Degenhardt, F. Dentener, D. C. Des Jarlais, K. Devries, M. Dherani, E. L. Ding, E. R. Dorsey, T. Driscoll, K. Edmond, S. E. Ali, R. E. Engell, P. J. Erwin, S. Fahimi, G. Falder, F. Farzadfar, A. Ferrari, M. M. Finucane, S. Flaxman, F. G. R. Fowkes, G. Freedman, M. K. Freeman, E. Gakidou, S. Ghosh, E. Giovannucci, G. Gmel, K. Graham, R. Grainger, B. Grant, D. Gunnell, H. R. Gutierrez, W. Hall, H. W. Hoek, A. Hogan, H. D. Hosgood, D. Hoy, H. Hu, B. J. Hubbell, S. J. Hutchings, S. E. Ibeanusi, G. L. Jacklyn, R. Jasrasaria, J. B. Jonas, H. Kan, J. a. Kanis, N. Kassebaum, N. Kawakami, Y.-H. Khang, S. Khatibzadeh, J.-P. Khoo, C. Kok, F. Laden, R. Lalloo, Q. Lan, T. Lathlean, J. L. Leasher, J. Leigh, Y. Li, J. K. Lin, S. E. Lipshultz, S. London, R. Lozano, Y. Lu, J. Mak, R. Malekzadeh, L. Mallinger, W. Marcenes, L. March, R. Marks, R. Martin, P. McGale, J. McGrath, S. Mehta, G. a. Mensah, T. R. Merriman, R. Micha, C. Michaud, V. Mishra, K. Mohd Hanafiah, A. a. Mokdad, L. Morawska, D. Mozaffarian, T. Murphy, M. Naghavi, B. Neal, P. K. Nelson, J. M. Nolla, R. Norman, C. Olives, S. B. Omer, J. Orchard, R. Osborne, B. Ostro, A. Page, K. D. Pandey, C. D. H. Parry, E. Passmore, J. Patra, N. Pearce, P. M. Pelizzari, M. Petzold, M. R. Phillips, D. Pope, C. A. Pope, J. Powles, M. Rao, H. Razavi, E. a. Rehfuess, J. T. Rehm, B. Ritz, F. P. Rivara, T. Roberts, C. Robinson, J. a. Rodriguez-Portales, I. Romieu, R. Room, L. C. Rosenfeld, A. Roy, L. Rushton, J. a. Salomon, U. Sampson, L. Sanchez-Riera, E. Sanman, A. Sapkota, S. Seedat, P. Shi, K. Shield, R. Shivakoti, G. M. Singh, D. a. Sleet, E. Smith, K. R. Smith, N. J. C. Stapelberg, K. Steenland, H. Stöckl, L. J. Stovner, K. Straif, L. Straney, G. D. Thurston, J. H.

Tran, R. Van Dingenen, A. van Donkelaar, J. L. Veerman, L. Vijayakumar, R. Weintraub, M. M. Weissman, R. a. White, H. Whiteford, S. T. Wiersma, J. D. Wilkinson, H. C. Williams, W. Williams, N. Wilson, A. D. Woolf, P. Yip, J. M. Zielinski, A. D. Lopez, C. J. L. Murray, M. Ezzati, M. a. AlMazroa, and Z. a. Memish, "A comparative risk assessment of burden of disease and injury attributable to 67 risk factors and risk factor clusters in 21 regions, 1990-2010: a systematic analysis for the Global Burden of Disease Study 2010.," *Lancet*, vol. 380, pp. 2224–60, Dec. 2012.

[9] M. Johnson, R. Edwards, C. Alatorre Frenk, and O. Masera, "In-field greenhouse gas emissions from cookstoves in rural Mexican households," *Atmospheric Environment*, vol. 42, pp. 1206–1222, 2008.

[10] R. Yevich and J. A. Logan, "An assessment of biofuel use and burning of agricultural waste in the developing world," *Global Biogeochemical Cycles*, vol. 17, Dec. 2003.

[11] O. Boucher, D. Randall, P. Artaxo, C. Bretherton, G. Feingold, P. Forster, V.-M. Kerminen, Y. Kondo, H. Liao, U. Lohmann, P. Rasch, S. Satheesh, S. Sherwood, B. Stevens, and X. Zhang, *Clouds and Aerosols. In: Climate Change 2013: The Physical Science Basis. Contribution of Working Group I to the Fifth Assessment Report of the Intergovernmental Panel on Climate Change.* Cambridge, United Kingdom and New York, NY, USA: Cambridge University Press, 2013.

[12] J. R. Pierce, M. J. Evans, C. E. Scott, S. D. D'Andrea, D. K. Farmer, E. Swietlicki, and D. V. Spracklen, "Weak global sensitivity of cloud condensation nuclei and the aerosol indirect effect to Criegee + SO¡sub¿2¡/sub¿ chemistry," *Atmospheric Chemistry and Physics*, vol. 13, pp. 3163–3176, Mar. 2013.

[13] D. V. Spracklen, K. S. Carslaw, U. Pöschl, a. Rap, and P. M. Forster, "Global cloud condensation nuclei influenced by carbonaceous combustion aerosol," *Atmospheric Chemistry and Physics*, vol. 11, pp. 9067–9087, Sept. 2011.

[14] S. E. Bauer, S. Menon, D. Koch, T. C. Bond, and K. Tsigaridis, "A global modeling study on carbonaceous aerosol microphysical characteristics and radiative effects," *Atmospheric Chemistry and Physics*, vol. 10, pp. 7439–7456, 2010.

[15] S. E. Bauer and S. Menon, "Aerosol direct, indirect, semidirect, and surface albedo effects from sector contributions based on the IPCC AR5 emissions for preindustrial and present-day conditions," *Journal of Geophysical Research*, vol. 117, p. D01206, Jan. 2012.

[16] M. Z. Jacobson, "Short-term effects of controlling fossil-fuel soot, biofuel soot and gases, and methane on climate, Arctic ice, and air pollution health," *Journal of Geophysical Research*, vol. 115, p. D14209, July 2010.

[17] R. J. Charlson, S. E. Schwartz, J. M. Hales, R. D. Cess, J. A. Coakley, J. E. Hansen, and D. J. Hofmann, "Climate forcing by anthropogenic aerosols.," *Science (New York, N.Y.)*, vol. 255, pp. 423–430, 1992.

[18] T. W. Kirchstetter, T. Novakov, and P. V. Hobbs, "Evidence that the spectral dependence of light absorption by aerosols is affected by organic carbon," *Journal of Geophysical Research D: Atmospheres*, vol. 109, 2004.

[19] G. R. McMeeking, E. Fortner, T. B. Onasch, J. W. Taylor, M. Flynn, H. Coe, and S. M. Kreidenweis, "Impacts of nonrefractory material on light absorption by aerosols emitted from biomass burning," *Journal of Geophysical Research: Atmospheres*, vol. 119, pp. 12,272–12,286, Nov. 2014.

[20] D. A. Lack, J. M. Langridge, R. Bahreini, C. D. Cappa, A. M. Middlebrook, and J. P. Schwarz, "Brown carbon and internal mixing in biomass burning particles.," *Proceedings of the National Academy of Sciences of the United States of America*, vol. 109, pp. 14802–7, Sept. 2012.

[21] R. Saleh, C. J. Hennigan, G. R. McMeeking, W. K. Chuang, E. S. Robinson, H. Coe, N. M. Donahue, and a. L. Robinson, "Absorptivity of brown carbon in fresh and photochemically aged biomass-burning emissions," *Atmospheric Chemistry and Physics*, vol. 13, pp. 7683–7693, Aug. 2013.

[22] R. Saleh, E. S. Robinson, D. S. Tkacik, A. T. Ahern, S. Liu, A. C. Aiken, R. C. Sullivan, A. A. Presto, M. K. Dubey, R. J. Yokelson, N. M. Donahue, and A. L. Robinson, "Brownness of organics in aerosols from biomass burning linked to their black carbon content," *Nature Geoscience*, vol. 7, no. August, pp. 647–650, 2014.

[23] M. O. Andreae and A. Gelencsér, "Black carbon or brown carbon? The nature of light-absorbing carbonaceous aerosols," 2006.

[24] J. H. Seinfeld and S. N. Pandis, *Atmospheric chemistry and physics: from air pollution to climate change*. New Yok: John Wiley & Sons, 1 ed., 2006.

[25] M. Z. Jacobson, "Strong radiative heating due to the mixing state of black carbon in atmospheric aerosols.," *Nature*, vol. 409, pp. 695–7, Feb. 2001.

[26] K. Klingmüller, B. Steil, C. Brühl, H. Tost, and J. Lelieveld, "Sensitivity of aerosol radiative effects to different mixing assumptions in the AEROPT 1.0 submodel of the EMAC atmospheric-chemistry–climate model," *Geoscientific Model Development*, vol. 7, pp. 2503–2516, 2014.

[27] M. Jacobson, "A physicallybased treatment of elemental carbon optics: Implications for global direct forcing of aerosols," *Geophysical Research Letters*, vol. 27, no. 2, pp. 217–220, 2000.

[28] T. C. Bond, G. Habib, and R. W. Bergstrom, "Limitations in the enhancement of visible light absorption due to mixing state," *Journal of Geophysical Research*, vol. 111, p. D20211, Oct. 2006.

[29] S. H. Chung and J. H. Seinfeld, "Climate response of direct radiative forcing of anthropogenic black carbon," *Journal of Geophysical Research*, vol. 110, p. D11102, 2005.

[30] J. R. Pierce and P. J. Adams, "Efficiency of cloud condensation nuclei formation from ultrafine particles," *Atmospheric Chemistry and Physics*, vol. 7, pp. 1367–1379, Feb. 2007.

[31] N. Riemer, M. West, R. A. Zaveri, and R. C. Easter, "Simulating the evolution of soot mixing state with a particleresolved aerosol model," *Journal of Geophysical Research*, vol. 114, p. D09202, May 2009.

[32] C. a. Roden, T. C. Bond, S. Conway, and A. B. O. Pinel, "Emission Factors and Real-Time Optical Properties of Particles Emitted from Traditional Wood Burning Cookstoves," *Environmental Science & Technology*, vol. 40, pp. 6750–6757, Nov. 2006.

[33] T. P. Ackerman and O. B. Toon, "Absorption of visible radiation in atmosphere containing mixtures of absorbing and nonabsorbing particles.," *Applied optics*, vol. 20, pp. 3661–3667, 1981.

[34] D. a. Lack and C. D. Cappa, "Impact of brown and clear carbon on light absorption enhancement, single scatter albedo and absorption wavelength dependence of black carbon," *Atmospheric Chemistry and Physics*, vol. 10, pp. 4207–4220, May 2010.

[35] J. Hansen, M. Sato, R. Ruedy, P. Kharecha, A. Lacis, R. Miller, L. Nazarenko, K. Lo, G. A. Schmidt, G. Russell, I. Aleinov, S. Bauer, E. Baum, B. Cairns, V. Canuto, M. Chandler, Y. Cheng, A. Cohen, A. Del Genio, G. Faluvegi, E. Fleming, A. Friend, T. Hall, C. Jackman, J. Jonas, M. Kelley, N. Y. Kiang, D. Koch, G. Labow, J. Lerner, S. Menon, T. Novakov, V. Oinas, J. Perlwitz, J. Perlwitz, D. Rind, A. Romanou, R. Schmunk, D. Shindell, P. Stone, S. Sun, D. Streets, N. Tausnev, D. Thresher, N. Unger, M. Yao, and S. Zhang, "Climate simulations for 1880-2003 with GISS modelE," *Climate Dynamics*, vol. 29, pp. 661–696, 2007.

[36] Q. Wang, R.-J. Huang, J. Cao, Y. Han, G. Wang, G. Li, Y. Wang, W. Dai, R. Zhang, and Y. Zhou, "Mixing State of Black Carbon Aerosol in a Heavily Polluted Urban Area of China: Implications for Light Absorption Enhancement," *Aerosol Science and Technology*, vol. 48, pp. 689–697, May 2014.

[37] C. F. Bohren and D. R. Huffman, *Absorption and scattering of light by small particles*, vol. 98. 1983.

[38] K. A. Fuller, W. C. Malm, and S. M. Kreidenweis, "Effects of mixing on extinction by carbonaceous particles," *Journal of Geophysical Research*, vol. 104, p. 15941, July 1999.

[39] R. Zhang, A. F. Khalizov, J. Pagels, D. Zhang, H. Xue, and P. H. McMurry, "Variability in morphology, hygroscopicity, and optical properties of soot aerosols during atmospheric processing.," *Proceedings of the National Academy of Sciences of the United States of America*, vol. 105, pp. 10291–10296, 2008.

[40] M. Schnaiter, H. Horvath, O. Möhler, K. H. Naumann, H. Saathoff, and O. W. Schöck, "UV-VIS-NIR spectral optical properties of soot and soot-containing aerosols," *Journal of Aerosol Science*, vol. 34, pp. 1421–1444, 2003.

[41] M. Schnaiter, C. Linke, O. Möhler, K. H. Naumann, H. Saathoff, R. Wagner, U. Schurath, and B. Wehner, "Absorption amplification of black carbon internally mixed with secondary organic aerosol," *Journal of Geophysical Research D: Atmospheres*, vol. 110, pp. 1–11, 2005.

[42] S. Twomey, "Pollution and the planetary albedo," *Atmospheric Environment (1967)*, vol. 8, no. 12, pp. 1251–1256, 1974.

[43] M. D. Petters and S. M. Kreidenweis, "A single parameter representation of hygroscopic growth and cloud condensation nucleus activity – Part 2: Including solubility," 2008.

[44] X. Li, S. Wang, L. Duan, J. Hao, and Y. Nie, "Carbonaceous aerosol emissions from household biofuel combustion in China," *Environmental Science and Technology*, vol. 43, pp. 6076–6081, 2009.

[45] C. L'Orange, M. DeFoort, and B. Willson, "Influence of testing parameters on biomass stove performance and development of an improved testing protocol," *Energy for Sustainable Development*, vol. 16, pp. 3–12, Mar. 2012.

[46] T. C. Bond, "A technology-based global inventory of black and organic carbon emissions from combustion," *Journal of Geophysical Research*, vol. 109, no. D14, p. D14203, 2004.

[47] J. Jetter, Y. Zhao, and K. Smith, "Pollutant emissions and energy efficiency under controlled conditions for household biomass cookstoves and implications for metrics useful in setting international test," *Environmental Science & Technology*, vol. 46, no. 19, pp. 10827–10834, 2012.

[48] C. a. Roden, T. C. Bond, S. Conway, A. B. Osorto Pinel, N. MacCarty, and D. Still, "Laboratory and field investigations of particulate and carbon monoxide emissions from

traditional and improved cookstoves," *Atmospheric Environment*, vol. 43, pp. 1170–1181, Feb. 2009.

[49] S. Janhäll, M. O. Andreae, and U. Pöschl, "Biomass burning aerosol emissions from vegetation fires: particle number and mass emission factors and size distributions," 2009.

[50] J. Tryner, B. D. Willson, and A. J. Marchese, "The effects of fuel type and stove design on emissions and efficiency of natural-draft semi-gasifier biomass cookstoves," *Energy for Sustainable Development*, vol. 23, pp. 99–109, Dec. 2014.

[51] A. L. Robinson, N. M. Donahue, M. K. Shrivastava, E. A. Weitkamp, A. M. Sage, A. P. Grieshop, T. E. Lane, J. R. Pierce, and S. N. Pandis, "Rethinking organic aerosols: semivolatile emissions and photochemical aging.," *Science (New York, N.Y.)*, vol. 315, pp. 1259–1262, 2007.

[52] A. P. Grieshop, J. M. Logue, N. M. Donahue, and A. L. Robinson, "Laboratory investigation of photochemical oxidation of organic aerosol from wood fires – Part 1: Measurement and simulation of organic aerosol evolution," 2009.

[53] C. J. Hennigan, M. A. Miracolo, G. J. Engelhart, A. A. May, A. A. Presto, T. Lee, A. P. Sullivan, G. R. McMeeking, H. Coe, C. E. Wold, W. M. Hao, J. B. Gilman, W. C. Kuster, J. De Gouw, B. A. Schichtel, J. L. Collett, S. M. Kreidenweis, and A. L. Robinson, "Chemical and physical transformations of organic aerosol from the photo-oxidation of open biomass burning emissions in an environmental chamber," *Atmospheric Chemistry and Physics*, vol. 11, pp. 7669–7686, 2011.

[54] G. Capes, B. Johnson, G. McFiggans, P. I. Williams, J. Haywood, and H. Coe, "Aging of biomass burning aerosols over West Africa: Aircraft measurements of chemical composition, microphysical properties, and emission ratios," *Journal of Geophysical Research*, vol. 113, p. D00C15, Oct. 2008.

[55] K. M. Sakamoto, J. D. Allan, H. Coe, J. W. Taylor, T. J. Duck, and J. R. Pierce, "Aged boreal biomass burning aerosol size distributions from BORTAS 2011," *Atmospheric Chemistry and Physics Discussions*, vol. 14, pp. 24349–24385, Sept. 2014.

[56] T. C. Bond and K. Sun, "Can reducing black carbon emissions counteract global warming?," *Environmental Science and Technology*, vol. 39, pp. 5921–5926, 2005.

[57] P. J. Adams and J. H. Seinfeld, "Predicting global aerosol size distributions in general circulation models," *Journal of Geophysical Research*, vol. 107, no. D19, p. 4370, 2002.

[58] Y. H. Lee and P. J. Adams, "A Fast and Efficient Version of the TwO-Moment Aerosol Sectional (TOMAS) Global Aerosol Microphysics Model," *Aerosol Science and Technology*, vol. 46, pp. 678–689, June 2012.

[59] Y. H. Lee, J. R. Pierce, and P. J. Adams, "Representation of nucleation mode microphysics in a global aerosol model with sectional microphysics," *Geoscientific Model Development*, vol. 6, pp. 1221–1232, 2013.

[60] J. G. J. Olivier, A. F. Bouwman, C. W. M. Van Der Maas, and J. J. M. Berdowski, "Emission database for global atmospheric research (EDGAR): Version 2.0," in *Studies in Environmental Science*, vol. 65, pp. 651–659, 1995.

[61] H. Kuhns, M. Green, and V. Etyemezian, "Big Bend Regional Aerosol and Visibility Observational (BRAVO) Study Emissions Inventory," vol. 89119, no. 702, 2003.

[62] D. G. Streets, T. Bond, G. R. Carmichael, S. Fernandes, Q. Fu, D. He, Z. Klimont, S. Nelson, N. Y. Tsai, M. Wang, J.-H. Woo, and K. Yarber, "An inventory of gaseous and primary aerosol emissions in Asia in the year 2000," *Journal of Geophysical Research*, vol. 108, no. D21, p. 8809, 2003.

[63] M. Auvray and I. Bey, "Long-range transport to Europe: Seasonal variations and implications for the European ozone budget," 2005.

[64] G. R. Van Der Werf, J. T. Randerson, L. Giglio, G. J. Collatz, M. Mu, P. S. Kasibhatla, D. C. Morton, R. S. Defries, Y. Jin, and T. T. Van Leeuwen, "Global fire emissions and the contribution of deforestation, savanna, forest, agricultural, and peat fires (1997-2009)," *Atmospheric Chemistry and Physics*, vol. 10, pp. 11707–11735, 2010.

[65] P. Chylek and J. Wong, "Effect of absorbing aerosols on global radiation budget," *Geophysical research letters*, vol. 22, no. 8, pp. 929–931, 1995.

[66] P. Köpke, M. Hess, I. Schult, and E. Shettle, *Global aerosol data set*. Max-Planck-Institut für Meteorologie Hamburg, Germany, 1997.

[67] J. M. Edwards and A. Slingo, "Studies with a flexible new radiation code. I: Choosing a comnfiguration for a large-scale model," *Quarterly Journal of the Royal Meteorological Society*, vol. 122, pp. 689–719, 1996.

[68] C. E. Scott, a. Rap, D. V. Spracklen, P. M. Forster, K. S. Carslaw, G. W. Mann, K. J. Pringle, N. Kivekäs, M. Kulmala, H. Lihavainen, and P. Tunved, "The direct and indirect radiative effects of biogenic secondary organic aerosol," *Atmospheric Chemistry and Physics*, vol. 14, pp. 447–470, Jan. 2014.

[69] A. Nenes, "Parameterization of cloud droplet formation in global climate models," *Journal of Geophysical Research*, vol. 108, no. D14, p. 4415, 2003.

[70] C. Fountoukis, "Continued development of a cloud droplet formation parameterization for global climate models," *Journal of Geophysical Research*, vol. 110, no. D11, p. D11212, 2005.

[71] J. Wang, M. J. Cubison, a. C. Aiken, J. L. Jimenez, and D. R. Collins, "The importance of aerosol mixing state and size-resolved composition on CCN concentration and the variation of the importance with atmospheric aging of aerosols," *Atmospheric Chemistry and Physics*, vol. 10, pp. 7267–7283, 2010.

[72] W. B. Rossow and R. A. Schiffer, "Advances in Understanding Clouds from ISCCP," *Bulletin of the American Meteorological Society*, vol. 80, pp. 2261–2287, 1999.

[73] H. Vehkamäki, "An improved parameterization for sulfuric acid–water nucleation rates for tropospheric and stratospheric conditions," *Journal of Geophysical Research*, vol. 107, no. D22, p. 4622, 2002.

[74] I. Napari, M. Kulmala, and H. Vehkamäki, "Ternary nucleation of inorganic acids, ammonia, and water," *Journal of Chemical Physics*, vol. 117, pp. 8418–8425, 2002.

[75] J. Jung, C. Fountoukis, P. J. Adams, and S. N. Pandis, "Simulation of in situ ultrafine particle formation in the eastern United States using PMCAMx-UF," *Journal of Geophysical Research*, vol. 115, p. D03203, Feb. 2010.

[76] D. M. Westervelt, J. R. Pierce, I. Riipinen, W. Trivitayanurak, a. Hamed, M. Kulmala, a. Laaksonen, S. Decesari, and P. J. Adams, "Formation and growth of nucleated particles into cloud condensation nuclei: model-measurement comparison," *Atmospheric Chemistry and Physics Discussions*, vol. 13, pp. 8333–8386, Mar. 2013.

[77] S. D. D'Andrea, S. a. K. Häkkinen, D. M. Westervelt, C. Kuang, E. J. T. Levin, V. P. Kanawade, W. R. Leaitch, D. V. Spracklen, I. Riipinen, and J. R. Pierce, "Understanding global secondary organic aerosol amount and size-resolved condensational behavior," *Atmospheric Chemistry and Physics*, vol. 13, pp. 11519–11534, Nov. 2013.

[78] D. V. Spracklen, J. L. Jimenez, K. S. Carslaw, D. R. Worsnop, M. J. Evans, G. W. Mann, Q. Zhang, M. R. Canagaratna, J. Allan, H. Coe, G. McFiggans, A. Rap, and P. Forster, "Aerosol mass spectrometer constraint on the global secondary organic aerosol budget," *Atmospheric Chemistry and Physics*, vol. 11, pp. 12109–12136, 2011.

[79] A. P. Grieshop, J. D. Marshall, and M. Kandlikar, "Health and climate benefits of cookstove replacement options," *Energy Policy*, vol. 39, pp. 7530–7542, Dec. 2011.

[80] A. L. Robinson, A. P. Grieshop, N. M. Donahue, and S. W. Hunt, "Updating the Conceptual Model for Fine Particle Mass Emissions from Combustion Systems Allen L. Robinson," *Journal of the Air & Waste Management Association*, vol. 60, pp. 1204–1222, Oct. 2010.

[81] J. R. Pierce, G. Theodoritsi, P. J. Adams, and S. N. Pandis, "Parameterization of the effect of sub-grid scale aerosol dynamics on aerosol number emission rates," *Journal of Aerosol Science*, vol. 40, pp. 385–393, 2009.

[82] G. A. Ban-Weiss, M. M. Lunden, T. W. Kirchstetter, and R. A. Harley, "Size-resolved particle number and volume emission factors for on-road gasoline and diesel motor vehicles," *Journal of Aerosol Science*, vol. 41, pp. 5–12, 2010.

[83] S. K. Akagi, J. S. Craven, J. W. Taylor, G. R. McMeeking, R. J. Yokelson, I. R. Burling, S. P. Urbanski, C. E. Wold, J. H. Seinfeld, H. Coe, M. J. Alvarado, and D. R. Weise, "Evolution of trace gases and particles emitted by a chaparral fire in California," *Atmospheric Chemistry and Physics*, vol. 12, pp. 1397–1421, 2012.

[84] S.-L. Sihto, M. Kulmala, V.-M. Kerminen, M. Dal Maso, T. Petäjä, I. Riipinen, H. Korhonen, F. Arnold, R. Janson, M. Boy, A. Laaksonen, and K. E. J. Lehtinen, "Atmospheric sulphuric acid and aerosol formation: implications from atmospheric measurements for nucleation and early growth mechanisms," *Atmospheric Chemistry and Physics*, vol. 6, pp. 4079–4091, Sept. 2006.

[85] A. V. Donkelaar, R. V. Martin, M. Brauer, and B. L. Boys, "Use of Satellite Observations for Long-Term Exposure Assessment of Global Concentrations of Fine Particulate Matter," *Environmental health perspectives*, vol. 123, no. 2, pp. 135–143, 2015.

[86] A. Rap, C. E. Scott, D. V. Spracklen, N. Bellouin, P. M. Forster, K. S. Carslaw, A. Schmidt, and G. Mann, "Natural aerosol direct and indirect radiative effects," *Geophysical Research Letters*, vol. 40, pp. 3297–3301, 2013.

[87] G. Legros, I. Havet, N. Bruce, and S. Bonjour, "The Energy Access Situation in Developing Countries. World Health Organization and UNDP," 2009.

[88] D. Shindell, J. C. I. Kuylenstierna, E. Vignati, R. van Dingenen, M. Amann, Z. Klimont, S. C. Anenberg, N. Muller, G. Janssens-Maenhout, F. Raes, J. Schwartz, G. Faluvegi, L. Pozzoli, K. Kupiainen, L. Höglund-Isaksson, L. Emberson, D. Streets, V. Ramanathan, K. Hicks, N. T. K. Oanh, G. Milly, M. Williams, V. Demkine, and D. Fowler, "Simultaneously mitigating near-term climate change and improving human health and food security.," *Science (New York, N.Y.)*, vol. 335, pp. 183–9, 2012.

[89] A. Hodzic, C. Wiedinmyer, D. Salcedo, and J. L. Jimenez, "Impact of trash burning on air quality in Mexico City," *Environmental Science and Technology*, vol. 46, no. 9, pp. 4950–4957, 2012.

[90] C. Wiedinmyer, R. J. Yokelson, and B. K. Gullett, "Global emissions of trace gases, particulate matter, and hazardous air pollutants from open burning of domestic waste.," *Environmental science & technology*, vol. 48, no. 16, pp. 9523–30, 2014.

[91] R. M. Healy, N. Riemer, J. C. Wenger, M. Murphy, M. West, L. Poulain, A. Wiedensohler, I. P. O'Connor, E. McGillicuddy, J. R. Sodeau, and G. J. Evans, "Single particle diversity and mixing state measurements," *Atmospheric Chemistry and Physics*, vol. 14, pp. 6289–6299, June 2014.

[92] N. Riemer and M. West, "Quantifying aerosol mixing state with entropy and diversity measures," *Atmospheric Chemistry and Physics*, vol. 13, pp. 11423–11439, Nov. 2013.